

Carl Einar Bonnevie Rasmussen

Risk-Influenced Path Planning based on Online Risk Analysis, Bayesian Networks and the A* Path Planning Algorithm

Master's thesis in Marine Technology

Supervisor: Asgeir Johan Sørensen

August 2019

Carl Einar Bonnevie Rasmussen

Risk-Influenced Path Planning based on Online Risk Analysis, Bayesian Networks and the A* Path Planning Algorithm

Master's thesis in Marine Technology
Supervisor: Asgeir Johan Sørensen
August 2019

Norwegian University of Science and Technology
Faculty of Engineering
Department of Marine Technology



Norwegian University of
Science and Technology

DEPARTMENT OF MARINE TECHNOLOGY

MASTER THESIS, MARINE CYBERNETICS

AUTONOMY AND RISK

Risk-Influenced Path Planning based on Online Risk Analysis, Bayesian Networks and the A* Path Planning Algorithm

Author

Carl Einar Bonnevie
Rasmussen

Supervisor

Prof. Asgeir J. Sørensen

Co-supervisor

PhD. Børge Rokseth

August 26, 2019



Faculty of Engineering

Department of Marine Technology

MASTER THESIS IN MARINE CYBERNETICS

SPRING 2019

FOR

STUD. TECHN. CARL EINAR BONNEVIE RASMUSSEN

**"Risk-Influenced Path Planning based on Online Risk Analysis,
Bayesian Networks and the A* Path Planning Algorithm"****Work description**

Different levels of autonomy has had a place in our daily lives and in different industries since the industrial revolution. Norway, with its high labour costs, is currently embracing it. This is also the case along the coast, where projects such as "Autoferry" and "Yara Birkeland" are aiming to make the transportation of people and goods more efficient every day.

The aim of this master thesis is to contribute to the research base of autonomous ships by providing a simple solution for risk-influenced pathfinding. This is done by building upon the foundation of online, simulation-based risk methodology. The work is tested through a simulation study of the research vessel RV Gunnerus navigating through a Norwegian fjord by the aid of the integration of online risk analysis, bayesian networks and the A* path finding algorithm.

Scope of work

1. Investigation of risk inducing factors found in a literature review provide static risk variability based on vessel characteristics.
2. Refinement of a risk model used in a prior implementation of OCA by the inclusion of Bayesian Networks.
3. Design of a system that predicts the risk of a marine vessel in transit within a real-world scenario and replans the vessels path in cases of high risk.
4. Design of a simulation study testing the systems capabilities.

Tentative project plan as of 21.02.2019

Task / Week no.	10	11	12	13	14	15	16	17	18	19	20	21	22	23	24	25	26	27
Correct errors in simulator	x																	
Improve risk model by implementing BBN		x	x															
Research and implement dynamic ship domains					x	x												
Research and improve modelling of environmental forces								x	x									
Research and make dynamic path planner											x	x						
Conduct case new case studies														x				
Experiments at lab															x	x		
Report writing				x			x			x			x				x	x

The report shall be written in English and edited as a research report including literature survey, description of mathematical models, description of control algorithms, simulation results, model test results, discussion and a conclusion including a proposal for further work. Source code should be provided. It is supposed that the Department of Marine Technology, NTNU, can use the results freely in its research work, unless otherwise agreed upon, by referring to the student's work.

The thesis should be submitted within 26. August.

Supervisor: Asgeir Johan Sørensen

Co-supervisor: Børge Rokseth

Abstract

The work presented in this master thesis attempt to contribute to the base of knowledge for autonomous marine vessels by offering a suggestion for functionality in an autonomous vessels system architecture. The functionality is based on the integration of a bayesian network into a framework for online risk analysis and using the predicted risk to trigger a A* path planner in order to make a safer path. The work is of importance because awareness of risk is highly relevant for higher levels of autonomy.

Sammendrag

Arbeidet presentert i denne masteroppgaven forsøker å bidra til kunnskapsgrunnlaget for autonome marine fartøy ved å tilby forslag til funksjonalitet i et autonomt fartøys kontrollarkitektur. Funksjonaliteten er basert på integreringen av et bayesiansk nettverk inn i et rammeverk for sanntids risikoanalyse og for å så bruke den predikerte risikoen for å starte en A* ruteplanlegger med hensikt til å lage en tryggere rute. Arbeidet er viktig av den grunn at bevissthet rundt risiko er høyst relevant for høyere nivåer av autonomi.

Acknowledgements

The author would like to express gratitude to the supervisors of the thesis. First, Asgeir J. Sørensen's optimism, expertise and availability has been greatly appreciated. It took some time to shape the contents of the work and during this time he was both encouraging and demanding for progression. It is obvious to the author that the head of AMOS¹ cares a great deal about his students, as he pushes in time for them in what seems an overfilled schedule with travels, lectures, meetings and more. Second, the author would like to thank Børge Rokseth. In between his work as a post. doc he has been a invaluable discussion partner and given valuable lessons in how to explain and present ones work. His unparalleled availability, pragmatic and down to earth personality and belief in his, at times, desperate student has made him easy to approach and to talk to and provided motivation in times of need. No question, ever how stupid, have been frowned upon. The author believes these qualities are of outmost importance to any supervisor and educator. The supervision of these two professionals has exceeded the authors expectations in every manner and future students would be lucky to acquire their aid. Even though the author's work is far from close to pay any justice to the level of their guidance it is hoped that it at least might be of some use in some way or another.

The author would also like to thank PhD. student Einar Ueland for his help with the implementation of the A* path finding algorithm and post doc. Christoph Alexander Tieme for his tips on implementing the bayesian network.

Some of the author's fellow students are also well deserving some proper acknowledgement. In particular, Erlend Lundby, Tobias Torben and Håkon Teigland has offered great assistance as discussion partners regarding different kinds of programming. Erlend and Are Wahlstrøm also served a crucial role as editors on the final day before delivery.

No acknowledgement is complete without a mention to the author's closest supporters - his family. A huge thank you goes to Nadia, the author's girlfriend, Julie, his sister, and Maren, his mom. The care these people has shown has been greatly appreciated.

¹ Centre for Autonomous Marine Operations and Systems, a cooperation between the Department of Marine Technology and the Department of Engineering Cybernetics at the Norwegian University of Science and Technology

A final acknowledgement will be given to "BayesFusion, LLC" for providing the free use of their software for bayesian networks - GeNie Modeler and SMILE Engine. Their software is available at <http://www.bayesfusion.com/>.

Table of Contents

Abstract	i
Sammendrag	ii
Acknowledgements	iii
1 Introduction	1
1.1 Motivation and background	1
1.2 Research question and work description	2
1.3 Simulator prerequisites	3
2 Previous work	5
2.1 Marine accidents, causes and risk influencing factors	5
2.2 Situation awareness for ships and unmanned surface vehicles	8
2.3 A framework for online consequence analysis	8
2.4 Mathematical modelling	12
2.4.1 Kinematics	12
2.4.2 Kinetics	15
2.4.3 Heading and speed control	18
2.5 Appliance of a eletronic map	19
2.6 Guidance system	22
2.6.1 The A* path planning algorithm	22
2.6.2 Line-of-Sight path following	24
2.7 Bayesian Belief Networks	27
3 Method	29
3.1 The OCA simulator	30
3.1.1 Bayesian Network	32
3.2 Guidance	34
3.2.1 A* - the path planning algorithm	34
4 Results	39
4.1 Validation	39
4.1.1 Vessel model and environment	39
4.1.2 OCA	43

4.1.3	Bayesian network	49
4.1.4	A^*	51
4.2	Combining the parts	52
5	Discussion	57
5.1	Further work	58
6	Conclusion	61
	List of Figures	63
	List of Tables	65
	Bibliography	67
A	Tables	71

Chapter 1

Introduction

1.1 Motivation and background

This section justifies the later research questions through an example and presents the thought processes forming the thesis.

In march 2019 a cruise vessel known as "Viking Sky" lost propulsion during a storm in Hustadvika, Møre and Romsdal county, Norway. For the people living nearby, Hustadvika is known for its numerous awash rocks and history with accidents. Yet, the vessel with its cargo of approximately 1400 people departed its harbour with the belief that the vessel could ride off the storm. After facing the emergency situation of propulsion loss during the storm, Viking Sky dropped its two anchors in fear of stranding. At first the anchors did not connect with the sea floor. The vessels passengers soon thereafter required helicopter support in order to be evacuated, as no other nearby vessels could take the risk of coming to its rescue. Luckily, after half an hour the anchors connected with the sea floor and a potential disaster was avoided.

This event illustrates the fact that most accidents at sea is caused or is influenced by human error (Chauvin et al., 2013). It also illustrates a problem with decision making and risk - how can one rationally evaluate the risk of a similar situation?

Computer programs are able to generate and analyse large amounts of data in a short amount of time. This enables the possibility of utilising computer programs to evaluate risk and suggest safe routes given a certain operation with certain conditions during the operation. This lays the foundation for more robust decision making as it provides valuable information for the captain to base his or her decision upon. Implementing these kinds of computer programs moves the industry one step closer to autonomy as these programs can assist in safe autonomous operations.

A key feature of autonomous systems is some kind of situation awareness, which loosely defined is the understanding of the surrounding environment. Situation awareness can be regarded as a combination of the first three points in the definition of autonomy - sensing, perception and analysis. A more formal and precise definition is given by Endsley (1988), which describes situation awareness as "*the perception of the elements in the environment within a volume of time and space, the comprehension of their meaning, and the projection of their status in the near future*".

The concept of risk is often integrated into the understanding of the environment, even though it is not an explicit part of the formal definition of situation awareness. Dynamic risk assesment with regards to motion planning is discussed in Wardzinski (2008), which presents a simple model based on the distance to a nearby vehicle. In Section 3 he comments on the need for situation awareness and in Section 4 the problem of predicting future situations.

1.2 Research question and work description

The research question of the thesis is "*Can a ship's probabilities for partial system failure be updated automatically during the ship's transit due and can the risk of system failure be used to suggest new, safer routes?*".

Work description

The work done in this thesis consists of proposing and testing functionality to components in an autonomous system.

Scope of work

1. Investigation of risk inducing factors found in a literature review provide static risk variability based on vessel characteristics.
2. Refinement of a risk model used in a prior implementation of OCA by the inclusion of Bayesian Networks.
3. Design of a system that predicts the risk of a marine vessel in transit within a real-world scenario and replans the vessels path in cases of high risk.
4. Design of a simulation study testing the systems capabilities.

Theoretical background behind a simulator. The simulator is consisting of vessel dynamics (movements of vessel), environment (geometry, forces), risk analysis based on a bayesian network and the vessels control system. tries to first quantify the likelihood of certain types of hazardous events to occur, i.e loss of motor power, and secondly (to a small extent) calculate the consequences of the hazardous event.

1.3 Simulator prerequisites

In order to recreate the results in this thesis, a few tools are necessary. The code is written in the high level Matlab programming language, which is compiled by the integrated development environment (IDE) by the same name. This is a commercial platform from MathWorks, which also provides Simulink. Simulink is a graphical programming environment for simulation of dynamical systems that also is used in this thesis. A couple of the functions used are from the map and aerospace toolboxes in Matlab, that also is provided by MathWorks. Also, the open source marine systems simulator (mss) toolbox is used with the mentioned products from MathWorks to conduct simulations. The code is written for a map in the shapefile format, and has in this case is provided by Kartverket. The software used to model the bayesian network is named GeNIe Modeler and SMILE Engine and can be used for academic purposes free of charge at <http://www.bayesfusion.com/>. Lastly, the used vessel model is named R/V Gunnerus and is provided by NTNU.

Chapter 2

Previous work

The purpose of this chapter is to summarise necessary background material and previous work related to online consequence analysis of autonomous ships. More elaborate information of some of the contents can be found in Rasmussen (2019); Fossdal (2018).

The chapter starts with a literature search of causes to marine accidents. The search starts wide, looking at general causes to general accidents, before narrowing down to accidents in Norwegian waters, and lastly looking at ferries in Norwegian waters specifically. The goal of the review is to identify risk inducing factors to be used in an online consequence analysis. Section 2.3 first examines the literature for solutions for online risk analysis, before presenting a framework proposed by (Fossdal, 2018). The mathematical foundation for a vessel simulator is presented in Section 2.4. Following the mathematical foundation is the addition of electronic sea charts, which are laid fourth in Section 2.5. This is based on the work of (Rasmussen, 2019). Section 2.6 explains the theory behind the path finding logic of A*. A* is an algorithm widely used in video games to find the shortest path, but as this Section shows it can also be used for other criterias. Lastly, this chapter presents bayesian belief networks in Section 2.7. These networks mimics how humans make decisions, and makes it possible for the autonomous vessel to update its probabilities for risk given changes in its environment.

2.1 Marine accidents, causes and risk influencing factors

In order to improve the functionality of the online consequence analysis simulator, it is wise to be aware of the most common causes to accidents. In this subsection, a small investigation of causes to marine accidents is conducted.

This subsection first clarifies the term risk inducing factors, before moving to find

some common denominators in ship accidents worldwide. It is easy to get a grim picture of the future after reading about causes to accidents, so a look on the trend of accidents at sea is given. Lastly, statistics from Norwegian naval accidents are given, in order to identify if Norway in any way differentiates itself compared to the rest of the world with regards to accidents. This structure is chosen in order to give a top-down perspective, starting with accidents in general and then narrowing down to ferries in Norwegian waters and fjords.

A central term is *risk influencing factors* (RIFs). (Hokstad et al., 2001) defines RIFs as relatively stable factors affecting the risk for an activity. Further elaboration on the term is given by (Rausand, 2011) - "*a RIF is not an isolated event but an enduring condition that influences the occurrence of hazardous events and the performance of the [protective risk] barriers*". In other words, RIFs represent something lasting that affect how often accidents happens. It is worth noting that the definition of RIFs does not communicate the time-frame of how it is

According to Cariou et al. (2008), vessel age, ship type and flag of registry appears to significant predictors of how often vessels collide. Table A.1 in Appendix A shows the results the authors extracted with data from the Swedish Maritime Administration in the period 1996-2001. A surprising finding was that vessels in the age group [20,30) years are more frequently found with deficiencies under inspection (28.8%) than vessels in the age group [30, ∞)(18.2%). Cariou et al. suggests that this might be because of "*a selection effect that implies that only extremely well maintained vessels older than 30 years still remain in operation*". (Harati-Mokhtari et al., 2007) looks at human factors, and claims that 80-85% of all recorded maritime accidents are directly caused by, or attributed to, a degree of human error. A similar number is also given by Rothblum (2006), which writes that human error is involved in 75-96%. It might indeed seem that human factors are important for accidents at sea, and (Chauvin et al., 2013) researched this further. By applying a modified version of the Human Factors Analysis and Classification System (HFACS), they showed that most collisions after 1998 are due to human decision errors. They also highlight factors that contribute to decision errors. These are poor visibility, misuse of instruments, loss of situation awareness and deficits in intership communications.

According to (Knudsen and Hassler, 2010) maritime accidents worldwide in the past decades are decreasing measured by total losses per thousand vessels. This is backed up by (ACGS), which based on data from Lloyd's Register has found the percentage lost of the world year in 25 year intervals from 1910. Even though

Year	1910	1935	1960	1985	2009
Percentage of world fleet lost	0.97%	0.69%	0.47%	0.40%	0.15%
Period growth	-	-28.9%	-31.9%	-14.8%	-37.5%

Table 2.1: Percentage of world fleet lost every 25th year from 1910. Source: (ACGS)

less accidents happen today, a single accident might be more costly due to high competition in the markets, loss of reputation and other alternative costs.

In 2015, a report from the "*national ship risk model*"-project were released (Stornes, 2015). This is an exploratory statistical analysis of incidents in Norwegian waters in the period 1981-2014 and is based on the Norwegian Maritime Authority's (NMA) database for incidents. It shows that the by far most frequent type of accidents for ferries are allisions (48.8%), followed by groundings (11.6%). It also looks at different types of environmental factors behind these types of accidents. (Rasmussen, 2019) extrapolates these data to make a table of lighting conditions for the route where the simulation study is conducted. Rasmussen (2019) continues with a short

Lighting	Time	Allision	Grounding
Daylight	09:43 - 15.18	53.2%	35.5%
Twilight	08:42 - 09.43	7.6%	7.3%
	16:18 - 17:17	-	-

Table 2.2: Lighting conditions at winter solstice in Gudvangen. Percentages for allision and grounding are retrieved from Stornes (2015) and represent the accidents for all ship types in NMA's accident database. Retrieved from Rasmussen (2019)

commentary discussing the interpretation of the Table 2.2, writing that the statistics might be scewed as one can assume most ferries travel during daytime and that the captain of ferries has better knowledge of their waters as the route do not have much room for variation. In addition to lighting conditions, (Rasmussen, 2019) also has some mentionable arguments with regard to how wind affects accidents in fjords. The thought process is that one could think strong winds occur in fjords, making the vessel drift or loose control by the following high waves. Table 2.2 and

Wind force	fire/expl.	grounding	capsizing	collision	allision	total
Weak	24.1%	31.3%	20.9%	40.2%	29.0%	31.3%
Moderate	17.3%	22.2%	13.7%	21.4%	21.4%	14.4%
Strong	5.4%	18.1%	29.5%	6.9%	18.7%	15.5%
Unknown	53.3%	28.4%	36.0%	31.4%	38.0%	32.8%

Table 2.3: Distribution of wind force within accident types. Table 7.3.5 in Stornes (2015). N = 5997.

Table 2.3 must be interpreted with a good amount of scepticism, as Stornes (2015) discusses in chapter five in his report. Four reasons are mentioned, and the first is the particular challenge that all the data comes from an accident database. This means that one can not tell whether the conditions listed are substantially different between accidents and non-accidents. The second issue is that the assumption that the RIFs have a partly static nature, meaning RIFs that has caused accident previous years are the same RIFs that are causing accidents today. The third issue is regarding the quality of data for each accident in the database. It contains mainly quantitative data such as geography, weather conditions and vessel age, and only some qualitative data on events surrounding the accident. It is therefore only a

limited range of the causes of the accidents that are being communicated through the statistics. The fourth issue is the challenge of comparing accidents. As Stornes (2015) writes, "*... it is impossible to know whether a decrease in accidents is due to a decrease in traffic, or a true decrease due to improved security measures*". This is an obstacle for generalisation. A final and fifth issue is the one of specialising the results to the specific type of vessels, which in this case is fjord-crossing ferries. It may seem that it is reasonable to assume that at least thinner fjords and fjords sheltered from the sea are not very vulnerable to wind and waves, and that these to factors would be minor RIFs for fjord-crossing ferries. Meanwhile, factors such as lighting, vessel age and flag of registry might be considered, but with a small volume of research available it is likely early to draw conclusions. In order to be able work with the OCA simulator, the mentioned RIFs will still be used as an example.

2.2 Situation awareness for ships and unmanned surface vehicles

A quintessential ability of any autonomous system is to gather and interpret information about the systems surroundings. This ability is described by the term *situation awareness* (SA). This is defined by (Endsley, 1988) as *The perception of the elements in the environment within a volume of time and space, the comprehension of their meaning, and the projection of their status in the near future*". Note that this definition consists of three elements; prediction of future states, perceptions of present states and the comprehension of the present states.

Autonomous systems may use different tools and strategies to acquire SA. In order to perceive its surroundings it uses sensor systems. In order to comprehend its surroundings and to then act on its comprehension sophisticated algorithms are required.

2.3 A framework for online consequence analysis

Online consequence analysis (OCA) is a potential answer to Endsleys last element of situation awareness - comprehension. The term OCA means to investigate possible outcomes of a specific situation in real time, as an alternative to prior a mission has commenced or after it is completed. To the author's knowledge, there is very limited literature surrounding this subject, at least in a maritime context. When searching on Google Scholar, the searches *online consequence analysis* and *computer simulation + consequence analysis* did, at the time of writing, not produce any relevant results on the first two search pages. However, the search *dynamic consequence analysis* resulted in an article (Torstein I. Bø, 2016). This article presents simulations of different failure modes for a dynamic positioning vessel, with the purpose of determining whether the vessel can maintain its position and to what degree it succeeds. On NTNU's private library, the search *online consequence analysis* brings up the master thesis being the foundation for this thesis.

The rest of this section will be devoted to explain the previous work on online consequence analysis presented in (Fosssdal, 2018). First, the idea will be explained, followed up by the frameworks place in a motion control system.

The idea of OCA is illustrated in Figure 2.1. The idea is to avoid collision by simulating different failure modes and analyse the simulation results in order to get a increased understanding of the risk at a given time. A vechile's failure mode is defined as a non-intended fault that affects a vehicles operating capabilities in a negative manner, e.g. loss of power.

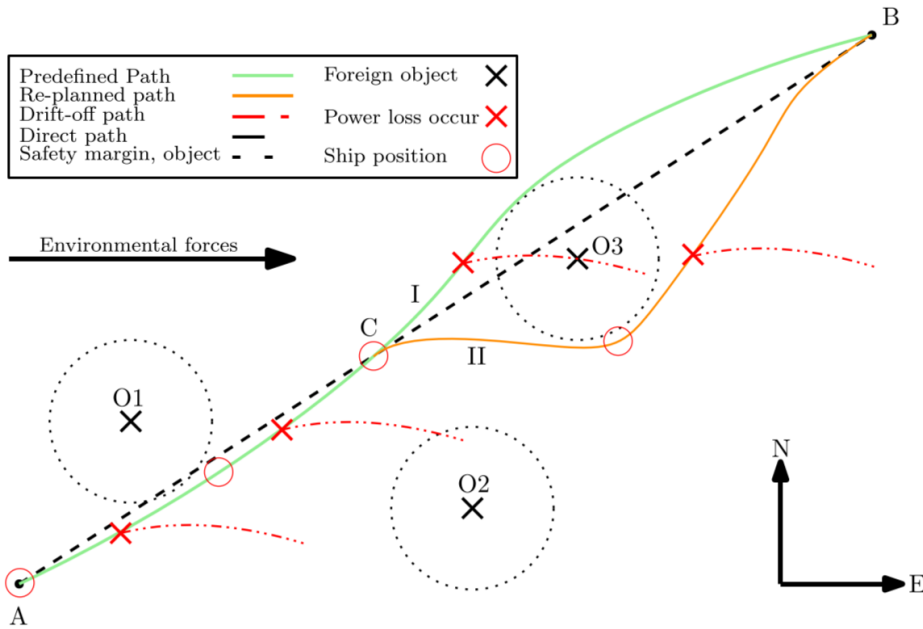


Figure 2.1: Illustration of the ambition of the OCA framework. Retrieved from Fosssdal (2018).

Here, a ship is travelling from point A to point B, through point C. Along its path are obstacles that must be avoided, marked by black X's with corresponding dotted circles outlining an area of potential risk of hitting the obstacle. During the vessels path OCA simulations takes place, marked by red circles. The simulations will calculate how the vessel will behave in case of some kind of failure mode, which in Figure 2.1 is illustrated by red X's which represent total blackout. In the case that one of the simulations indicate that the vessel is at considerable risk of hitting an obstacle, by for example crossing the dotted circle or hitting the obstacle directly, an alternative route will be planned. In addition, the risk of the failure mode will be calculated based on a consequence level which is determined by how close the simulated path is to an obstacle. The measure of risk is useful because it can be

compared against other metrics such as time spent and fuel, giving a foundation for awareness of what should be prioritised. In Figure 2.1 the alternative route is represented by the orange line, while the failure mode trajectory calculated by the OCA is the red dotted line.

A central question of the mentioned concept is how the collision risk is determined. This is done by multiplying the highest achieved consequence level (CL) during a failure mode simulation (FM) with the probability for that particular failure mode to occur, $P(FM_i)$. Lastly, the risk from each failure mode is added together to get the total quantitative risk, as defined by Varde and Pecht (2018):

$$R := \sum_i^k P(FM_i) \cdot CL_{FM_i, max} \quad (2.1)$$

The highest CL is determined by four steps. The first step is to calculate the distance from the vessel to all known obstacles during each time step of the simulation. This is defined in Equation (2.2). After all the distances has been computed, they are then compared to find the smallest one. In Equation (2.2c) below, $\bar{r}_{O_i}(h)$ is the distance from the vessel to the obstacle at timestep h , $\eta(h)$ is the vessels position at timestep h , and the subscripts N, E means "North" and "East", respectively. In Equation (2.2a) $\bar{\mathbf{r}}_{O, min}$ is a vector containing all the smallest distances to each obstacle during a simulation and lastly, m is the total number of time steps in a simulation.

$$\bar{\mathbf{r}}_{O, min} := [\bar{r}_{O1, min}, \bar{r}_{O2, min}, ..., \bar{r}_{On, min}] \quad (2.2a)$$

$$\bar{r}_{O_i, min} = \min\{\bar{r}_{O_i}(h)\}, \quad \forall h \in [1, m] \subset \mathcal{N} \quad (2.2b)$$

$$\bar{r}_{O_i}(h) = \sqrt{(\eta_N(h) - \eta_{O_i, N})^2 + (\eta_E(h) - \eta_{O_i, E})^2} \quad (2.2c)$$

The second step is to find which objects that has to be analysed further and found formalised in Equation (2.3). This is done by comparing the smallest distance $\bar{\mathbf{r}}_{O, min}$ with the largest consequence level radii R_{L1} . The consequence levels is determined from the distance to obstacle and each level has its own radii. The output is a boolean vector of the same size size as $\bar{\mathbf{r}}_{O, min}$, indicating which distances are worthy further analysis.

$$\bar{\mathbf{r}}_{O, min} < R_{L1} \quad (2.3a)$$

$$\bar{\mathbf{O}}_{rel} := [O1_{bool}, O2_{bool}, ..., On_{bool}] \quad (2.3b)$$

Step three is to construct a matrix \mathbf{VL} with information of level violation and the time the violation occurs. This is a $m \times n$ matrix, where m is the number of time steps and n is the number of obstacles. The violation matrix \mathbf{VL} is defined as

$$\mathbf{VL} := \begin{bmatrix} CL_{O1}(h) & CL_{O2}(h) & \dots & CL_{Ok}(h) \\ CL_{O1}(2h) & CL_{O2}(2h) & \dots & CL_{Ok}(2h) \\ \vdots & \vdots & \ddots & \vdots \\ CL_{O1}(mh) & CL_{O2}(mh) & \dots & CL_{Ok}(mh) \end{bmatrix} \quad (2.4)$$

The fourth and last step is to find the highest consequence level, CL_{max} that occurred during the failure mode analysis.

$$CL_{max} = \max\{\mathbf{V}\mathbf{L}\} \quad (2.5)$$

OCA in a control system To better understand the OCAs position in a motion control system, refer to the example in Figure 2.2.

Here, the inputs to the OCA is three signals - system initialisation, estimated

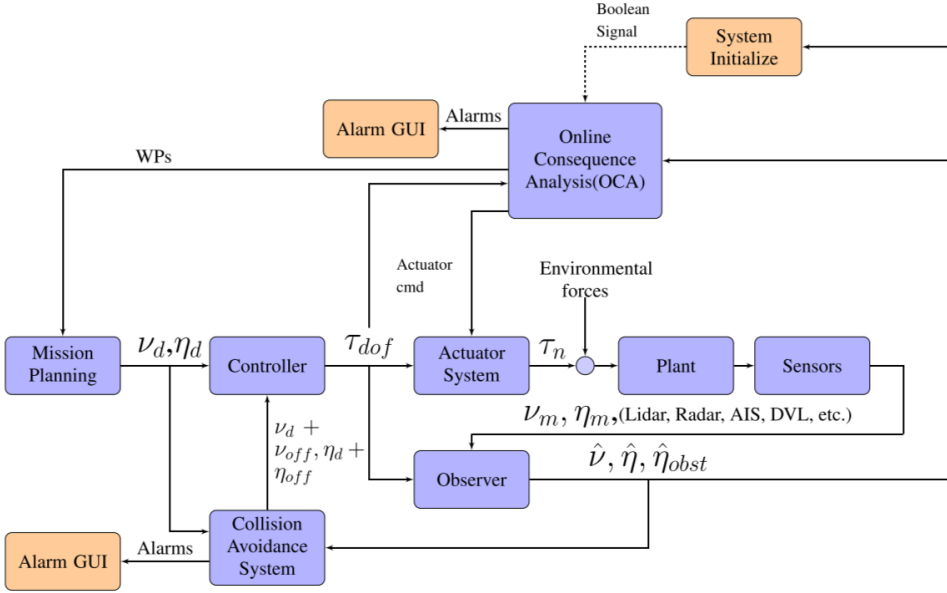


Figure 2.2: Motion control system with integrated OCA and collision avoidance. The symbols are later explained in Section 2.4. Retrieved from Fossdal (2018).

states from an observer and requested control forces. The system initialisation block decides in what circumstances the OCA should run, while the state estimates and control forces are needed to initialise the actual OCA simulations. Moving on to the example outputs of the OCA block, these are waypoints for mission planning, signals to the actuator system and alarm signals.

2.4 Mathematical modelling of marine vessels and environmental forces

This section summarises the mathematical relations used in the simulator. This includes kinematics, the geometrical aspects of motion, and the forces causing the motions, kinetics.

2.4.1 Kinematics

In order to describe the kinematics of the process plant model, it is advantageous to first present the different coordinate frames that are used. The information is retrieved from Fossen (2011).

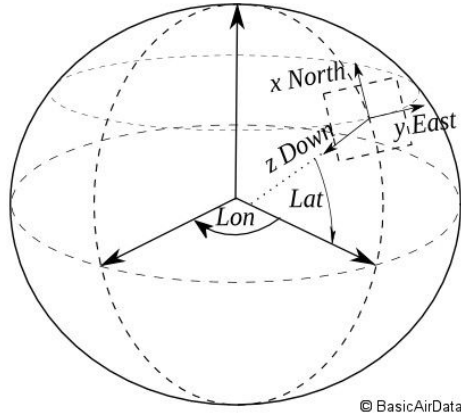


Figure 2.3: The relation between latitude and longitude in the NED frame. Retrieved from <https://www.basicairdata.eu>

Coordinate frames Figure 2.3 illustrates the definition of the *NED coordinate frame* $\{n\}$, which is a tangent plane on the surface of the earth. The x-axis of the NED frame points towards the true north of the globe, and the y-axis points directly east. The z-axis, down, points toward the center of the Earth. It is worth mentioning that per definition, the NED frame is not inertial. This implies that Newtons laws are not usable. However, when the tangential plane is small, it is common to assume that the plane is inertial. This approximation is valid when the longitude and latitude is constant, and is called flat earth navigation. This introduces longitude and latitude, which makes up a geographic coordinate system. The lines going east and west are called latitudes, and these are defined relative to the equator. Longitudes, on the other hand, goes vertically from south to north and are defined from the prime meridian (also known as the Greenwich Meridian), which is the curve from the north pole to the south pole that passes through the

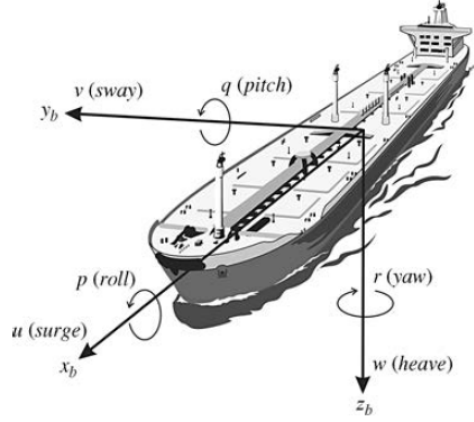


Figure 2.4: The body frame for a marine vessel, with linear position x_b , y_b and z_b , angular velocities p , q , r and linear velocities u , v , w . Retrieved from Fossen (2011).

Royal Observatory in Greenwich (GISGeography, 2019).

The *body frame* $\{b\}$ is a moving frame fixed to an object. Position and orientation is measured relative to an inertial frame, while velocity is expressed in body-fixed coordinate system.

The *flow frame* $\{c\}$ is used for calculating hydrodynamic forces, and the axes are found by rotating the body axes such that x_b is parallel to the fluid flow.

The notation from Fossen (2011) is used when describing the kinematics. This is best described by an example:

$\mathbf{p}_{b/n}^n$ Linear position of $\{b\}$ with respect to $\{n\}$ expressed in $\{n\}$.

Θ_{nb} Euler angles between the $\{n\}$ frame and the $\{b\}$ frame.

As it might yet be unclear what $\mathbf{p}_{b/n}^n$ means, the following Figure 2.5 is added to clarify.

Vessel kinematics In order to describe the vessel kinematics in the process plant, some definitions are needed. The linear and angular position vectors in the NED frame is described by

$$\mathbf{p}_{b/n}^n := \begin{bmatrix} N \\ E \\ D \end{bmatrix} \in \mathbb{R}^3 \quad \Theta_{nb} := \begin{bmatrix} \phi \\ \theta \\ \psi \end{bmatrix} \in \mathcal{S}^3 \quad (2.6)$$

In Equation (2.6), \mathbb{R}^3 is the three dimensional Euclidian space and \mathcal{S}^3 represent a sphere with Euler angles in the range $[0, 2\pi]$. The angles ϕ , θ and ψ represent

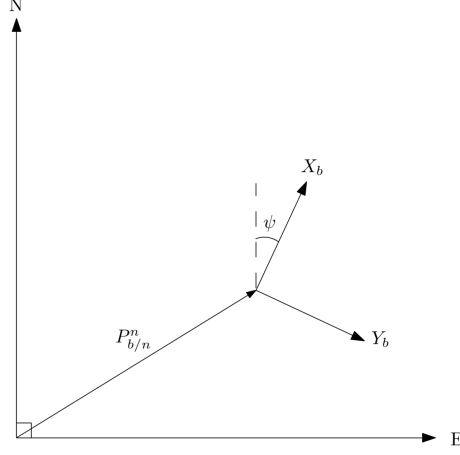


Figure 2.5: Illustration of the relationship between the NED frame and the body frame in 2D. X_b and Y_b are the x and y-directions in the body frame, respectively, while ψ is the yaw angle. Adapted from Fossdal (2018).

roll, pitch and yaw, respectively. The time derivatives of these angles can be seen in Figure 2.4.

The body fixed linear and angular velocities are described by

$$\mathbf{v}_{b/n}^b := \begin{bmatrix} u \\ v \\ w \end{bmatrix} \in \mathbb{R}^3 \quad \boldsymbol{\omega}_{b/n}^b := \begin{bmatrix} p \\ q \\ r \end{bmatrix} \in \mathbb{R}^3 \quad (2.7)$$

Here, u , v and w are the linear velocities in surge, sway and heave. The angular velocities has been explained above. Figure 2.4 serves as an illustration.

In order to make the final expression more compact, the state vectors are written as a combination of Equation (2.6) and Equation (2.7).

$$\boldsymbol{\eta} := \begin{bmatrix} \mathbf{p}_{b/n}^n \\ \boldsymbol{\Theta}_{nb} \end{bmatrix} \quad \boldsymbol{\nu} := \begin{bmatrix} \mathbf{v}_{b/n}^b \\ \boldsymbol{\omega}_{b/n}^b \end{bmatrix} \quad (2.8)$$

In order to rotate the body frame to the NED frame, two transformation matrices are needed. These represent the linear and angular velocity transformation from the body frame to the NED frame (Fossen, 2011).

$$\mathbf{R}_b^n(\boldsymbol{\Theta}_{nb}) = \begin{bmatrix} \cos \psi \cos \theta & -\sin \psi \cos \phi + \cos \psi \sin \theta \sin \phi & \sin \psi \sin \phi + \cos \psi \cos \phi \sin \theta \\ \sin \psi \cos \theta & \cos \psi \cos \phi + \sin \phi \sin \theta \sin \psi & -\cos \psi \sin \phi + \sin \theta \sin \psi \cos \phi \\ -\sin \theta & \cos \theta \sin \phi & \cos \theta \cos \phi \end{bmatrix} \quad (2.9a)$$

$$\mathbf{T}_\Theta(\Theta_{nb}) = \begin{bmatrix} 1 & \sin \phi \tan \theta & \cos \phi \tan \theta \\ 0 & \cos \phi & -\sin \phi \\ 0 & \sin \phi / \cos \theta & \cos \phi / \cos \theta \end{bmatrix} \quad \text{where } \theta \neq \pm \frac{\pi}{2} \quad (2.9b)$$

The vessel kinematics can now be described by the following equation.

$$\begin{bmatrix} \dot{\mathbf{p}}_{b/n}^n \\ \dot{\Theta}_{nb} \end{bmatrix} = \begin{bmatrix} \mathbf{R}_b^n(\Theta_{nb}) & \mathbf{0}_{3 \times 3} \\ \mathbf{0}_{3 \times 3} & T_\Theta(\Theta_{nb}) \end{bmatrix} \begin{bmatrix} \mathbf{v}_{b/n}^b \\ \boldsymbol{\omega}_{b/n}^b \end{bmatrix} \quad (2.10)$$

Finally, the vessel kinematics in Equation (2.10) can be written more compactly as

$$\dot{\boldsymbol{\eta}} = \mathbf{J}_\Theta(\boldsymbol{\eta})\boldsymbol{\nu} \quad (2.11)$$

2.4.2 Kinetics

This subsection has a top down approach starting with the complete model for the vessel dynamics. Afterwards, the single components of the model is looked into.

Complete manoeuvring model The complete model is a combination of the kinematics in Section 2.4.1 and the kinetics that are explained later in this subsection. This model is listed below

$$\dot{\boldsymbol{\eta}} = \mathbf{J}_\Theta(\boldsymbol{\eta})\boldsymbol{\nu} \quad (2.12a)$$

$$\mathbf{M}_{RB}\dot{\boldsymbol{\nu}} + \mathbf{M}_A\dot{\boldsymbol{\nu}}_r - \mathbf{C}_{RB}\boldsymbol{\nu} - \mathbf{C}_A\boldsymbol{\nu}_r - \mathbf{D}\boldsymbol{\nu}_r - \mathbf{d}(\boldsymbol{\nu}_r)\boldsymbol{\nu}_r - \mathbf{G}\boldsymbol{\eta} = \boldsymbol{\tau}_{exc}^b \quad (2.12b)$$

This equation is based on Newtons second law $\sum F = ma$ applied to a mass-damper-spring system, which is a common model describing the motions of a vessel. The mass matrices, $\{\mathbf{M}_{RB}, \mathbf{M}_A\} \in \mathbb{R}^{6 \times 6}$, are respectively the vessels inertia- and added mass matrices. The dampening matrices, $\{\mathbf{C}_{RB}, \mathbf{C}_A, \mathbf{D}, \mathbf{d}(\boldsymbol{\nu}_r)\} \in \mathbb{R}^{6 \times 6}$ are the Coriolis-centripetal, the Coriolis-centripetal contribution and the combined linear potential, linear viscous dampening matrix, respectively. Last on the left hand side are the spring force $\mathbf{g} \in \mathbb{R}^{6 \times 1}$, which is a vector of gravitational and/or buoyancy forces, and the vector \mathbf{g}_0 which represents pretrimming and ballast control forces and moments. On the right hand side displays the control force, $\boldsymbol{\tau}_{exc}^b$. Current is included implicitly by the relative velocities in the dampening terms. The relative velocity is defined in the body frame as the difference between the vessel velocity and the current velocity, or $\boldsymbol{\nu}_r = \boldsymbol{\nu}^b - \boldsymbol{\nu}_c^b$. Wind is not included.

Process plant *Process plant* models, also known as simulation models, is a "comprehensive description of the actual [physical] and should be as detailed as needed using high fidelity models" (Sørensen). Within the simulator, it is used to calculate the movement of the vessel within the main simulation. The applied process plant model has a underlying assumption of the ship always operating in deep water and that the vessel is completely rigid. The consequences of this assumption is not investigated further.

Below is the equation for the applied process plant model, based on Fossen (2011) and with incorporated cross-flow drag. Further elaboration can be found in Rasmussen (2019); Fossdal (2018).

$$\mathbf{M}_{RB}\dot{\boldsymbol{\nu}} + \mathbf{M}_A\dot{\boldsymbol{\nu}}_r + \mathbf{C}_{RB}(\boldsymbol{\nu})\boldsymbol{\nu} + \mathbf{C}_A(\boldsymbol{\nu}_r)\boldsymbol{\nu}_r + \mathbf{D}(\boldsymbol{\nu}_r)\boldsymbol{\nu}_r + \mathbf{g}(\boldsymbol{\eta}) + \mathbf{g}_0 + = \boldsymbol{\tau} + \boldsymbol{\tau}_{\text{wind}} + \boldsymbol{\tau}_{\text{wave}} \quad (2.13)$$

Linear manoeuvring model The linear manoeuvring model is used to calculate the vessels trajectory in the OCA and functions as a control plant model, which is a simplified process plant model made to lighten the computational burden and to run online opposed to offline. The linear maneuvering model is originally retrieved from (Perez and Fossen, 2007) and is listed below.

$$\mathbf{M}\dot{\boldsymbol{\nu}} + \mathbf{C}_{RB}\boldsymbol{\nu} + \mathbf{C}_A\boldsymbol{\nu} + \bar{\mathbf{B}}\boldsymbol{\nu} + \int_0^t \mathbf{K}(t-t')[\boldsymbol{\nu}(t')] + \mathbf{U}\mathbf{L}\boldsymbol{\eta}(t')dt' + \mathbf{G}\boldsymbol{\eta} = \boldsymbol{\tau}_{exc}^b + \bar{\boldsymbol{\tau}}^b \quad (2.14)$$

In this lightly rewritten equation, \mathbf{M} is defined as the sum of the inertia and added mass matrices, $\mathbf{M} = \mathbf{M}_{RB} + \mathbf{M}_A$. The Coriolis-centripetal force matrix is defined as $\mathbf{C}_{RB} = \mathbf{M}_{RB}\mathbf{U}\mathbf{L}$, where \mathbf{U} is the vessel speed and \mathbf{L} is a selection matrix. $\bar{\mathbf{B}}$ expresses linear potential flow dampening. The Coriolis-centripetal force gets an additional component from the added mass, namely \mathbf{C}_A . This is similarly defined, $\mathbf{C}_A = \mathbf{M}_A\mathbf{U}\mathbf{L}$. Next up, the convolution integral represents fluid memory effects, whereof \mathbf{K} is a retardation function. The fluid memory effects are *the change of fluid momentum due to the vessels motion at all subsequent times* according to Cummins (1962). Lastly, \mathbf{G} includes buoyancy and gravitational forces, $\boldsymbol{\tau}_{exc}^b$ represents external environmental forces such as waves and wind, in addition to control input, and $\bar{\boldsymbol{\tau}}^b$ is a constant potential dampening force defined by $\bar{\boldsymbol{\tau}}^b = \bar{\mathbf{B}}\bar{\boldsymbol{\nu}}$. The constant potential dampening $\bar{\mathbf{B}}$ will be moved over to the left hand side of the equation and into a linear dampening matrix.

Eq. (2.14) is valid for small turning rates and is based on potential theory and does therefore not include any viscous effects. To make the model more realistic, linear viscous dampening, nonlinear surge dampening and cross-flow drag is therefore added.

Linear viscous dampening Linear viscous dampening is added to the left hand side of Eq. (2.12). This type of dampening is mainly a result of the friction against the vessels hull, and is typically added to the linear potential dampening. Linear viscous dampening can be modelled as $\mathbf{B}_v\boldsymbol{\nu}$ where \mathbf{B}_v is the linear dampening coefficient. Usually, the total dampening of a vessel is modelled as the sum of a linear and nonlinear part

$$\mathbf{D}(\boldsymbol{\nu}_r) = \mathbf{D} + \mathbf{D}_{non}(\boldsymbol{\nu}_r) \quad (2.15)$$

where \mathbf{D} is the contribution from the potential and linear viscous dampening, while $\mathbf{D}_{non}(\boldsymbol{\nu}_r)$ includes the nonlinear dampening.

Nonlinear surge dampening This dampening component, also referred to as nonlinear surge resistance, can be modelled as by Lewis Lewis (1988) below

$$X = -\frac{1}{2} \rho S(1+k) C_f(u_r) |u_r| u_r \quad (2.16a)$$

$$C_f(u_r) = \underbrace{\frac{0.075}{(\log_{10}(Re) - 2)^2}}_{C_F} + C_R \quad (2.16b)$$

Here, ρ is the density of water, S is the wetted surface area and k is a form factor taking the geometry of the vessel into account¹. $C_f(u_r)$ consists of the flat plate friction coefficient C_F and the residual resistance, C_R , which is due to the hull's roughness, pressure resistance, wave-making and wave-breaking resistance. Re is the abbreviation of Reynolds number, an important coefficient in fluid dynamics. Lastly, u_r is the relative velocity in surge between the vessel and the incoming current.

Cross-flow drag In order to calculate the nonlinear dampening fore and moment in both sway and yaw, a cross-flow model is implemented. This is relevant for large relative current angles, expressed mathematically as $|\beta_c - \psi| \gg 0$ where β_c is the current's angle of attack and ψ is the heading of the vessel Fossen (2011). This is approached by strip theory, as showed by Faltinsen (1990).

$$Y = -\frac{1}{2} \rho \int_{-\frac{L_{pp}}{2}}^{\frac{L_{pp}}{2}} T(x) C_d^{2D} |v_r + xr| (v_r + xr) dx \quad (2.17a)$$

$$N = -\frac{1}{2} \rho \int_{-\frac{L_{pp}}{2}}^{\frac{L_{pp}}{2}} x T(x) C_d^{2D} |v_r + xr| (v_r + xr) dx \quad (2.17b)$$

In Eq. (2.17), Y and N is the force and moment in sway and yaw, respectively. The length between the vessels perpendiculars is L_{pp} and $T(x)$ is the vessels draft as a function of its length, while C_d^{2D} is the 2D drag coefficient. Lastly, $v_r = v - v_c$, is the relative velocity between the vessel and the current in sway.

The cross-flow principle is based on three assumptions Faltinsen (2005) that is not being discussed further;

1. The flow separates because of the cross-flow past the vessel.
2. The longitudinal velocity components do not influence the transverse forces on a cross section.
3. The transverse force on a cross section is mainly caused by separated flow effects on the pressure distribution around the vessel.

¹The form factor k is typically equal to 0.1 for a vessel in transit

2.4.3 Heading and speed control

This subsection provides the necessary background to perform simple PID control of a vessels heading and speed.

Autopilot The function of the autopilot is to keep the correct heading, ψ at all times. This is done by the use of a PID-controller, which is the most widespread controller in the industry due to its simplicity to implement and good performance. PID is an abbreviation for *proportional*, *integral* and *derivative* control.

$$\tau_N = -K_p \tilde{\psi} - C_{enable} \left(K_i \int_{t_0}^t \tilde{\psi}(T) dT \right) - K_d \dot{\tilde{\psi}} \quad (2.18a)$$

$$C_{enable} := \begin{cases} 1, & \text{if } |\tilde{\psi}| \leq \psi_{th} \\ 0, & \text{otherwise} \end{cases} \quad (2.18b)$$

In the equation above, τ_N is the commanded yaw force, $\tilde{\psi} = \psi - \psi_d$ is the heading error and $\{K_p, K_i, K_d\} > 0$ are the proportional gain, the integral gain and the derivative gain, respectively. C_{enable} is a term added in order to avoid integral windup, which would have happened during the change from one waypoint to another. In Eq. (2.18b), ψ_{th} is a specific threshold set to be larger than the steady state error of the system. When $C_{enable} = 1$, t_0 is set to the current time as this restarts the integral. This results in a controller which for large transients is controlled by the proportional and the derivative term with the integral term becoming active during steady state. Other simple, but yet more sophisticated solutions for solving the problem with integral wind-up can be found in Beard and McLain (2012).

Speed controller The speed controller obviously tries to make sure the speed of the vessel is where it should be. The control law is on the same form as the autopilot, but without derivative control. It is therefore called a PI-controller.

$$\tau_X = -K_p \tilde{U} - C_{enable} \left(K_i \int_{t_0}^t \tilde{U}(\tau) d\tau \right) \quad \text{where } K_p, K_i > 0 \quad (2.19a)$$

$$C_{enable} := \begin{cases} 1, & \text{if } |\tilde{U}| \leq U_{th} \\ 0, & \text{otherwise} \end{cases} \quad (2.19b)$$

$$U = \sqrt{u^2 + v^2} \quad (2.19c)$$

The above set of equations gives a control input τ_X in the heading direction, based on the speed error $\tilde{U} = U - U_d$ and the tuning of the parameters K_p and K_i . The switch parameter C_{enable} works in the same way as for the autopilot.

2.5 Appliance of a eletronic map

A electronic sea chart is implemented into the OCA framework in order to increase Endsleys first element of situation awareness - the perception of elements within the environment. When the vessels position is known, a map aids the vessel in identifying static elements in its vicinity. This section provides information of the map supplier, different kinds of map data and how it was used in addition to pre-processing of the map. The section is based on Rasmussen (2019).

The map and the map supplier The map was retrieved from The Norwegian Mapping Authority (NMA). This state-owned organization has the nationwide responsibility for making geographical information and supplied the digital map of the case area via their web portal, Geonorge.

The applied map is named *Sjøkart - Dybdedata* and contains unclassified depth data for planing, modelling, research and analytical purposes. The depth data is measured relative to the (vertical) chart datum. The *chart datum* is decided based on the lowest astronomical tide (LAT). LAT represents the lowest possible tide that has occurred during the last tide period of approximately 19 years under 'normal meteorological conditions' (Kartverket, 2018). As the meteorological conditions vary from Norway compared to other countries, the chart datum is therefore placed 20-30cm below LAT (Kartverket, 2018). The chart is was retrieved in the WGS84 format², which is used as a standard for georeference. Note that Sjøkart - Dybdedata is not an ENC (Electronic Navigational Chart), which is used in ECDIS (Electronic Chart Display and Information System), a device that is imposed by IMO (International Maritime Organization) on high-speed crafts since July 2008 Maratos (2008). The differences between the applied map and an equivalent ENC is the addition of light houses and other navigational information, as well as the organisation of the map on a national level and the resolution of the map (Jakobsen, 2019).

Table 2.4 contains the relevant information in the map that makes up the obstacles in the case studies. Figure 2.6 displays the map as it appears on NMAs website.

Processing After the map has been been downloaded in the shapefile format from the Norwegian Mapping Authority's online distribution service (Geonorge), the following steps were executed. The first step of processing was to crop the map over Sogn and Fjordane to the more manageable map over Aurlandsfjorden, where the case studies are taking place. This was needed as the map as a whole required more computer RAM than the authors personal computer had available. The second step was to extract relevant information from the map. This was data

²WGS84 is an abbreviation for World Geodetic System 1984.

Obstacle type	Meaning
Depths	Areas of varying water depth.
Underwater rock	Area of limited size that stretches toward the surface, but is more than 0.5m deeper than the chart datum.
Rock awash	Rock positioned down to 0.5m below chart datum.
Coastal contour	The coastline (shoreline) is defined from mean high water, or the average of all high tides during a tide period.
Drying heights	The area extending from the coastline to 0.5m below chart datum.

Table 2.4: Map information defining the obstacles. Source: Geonorge.

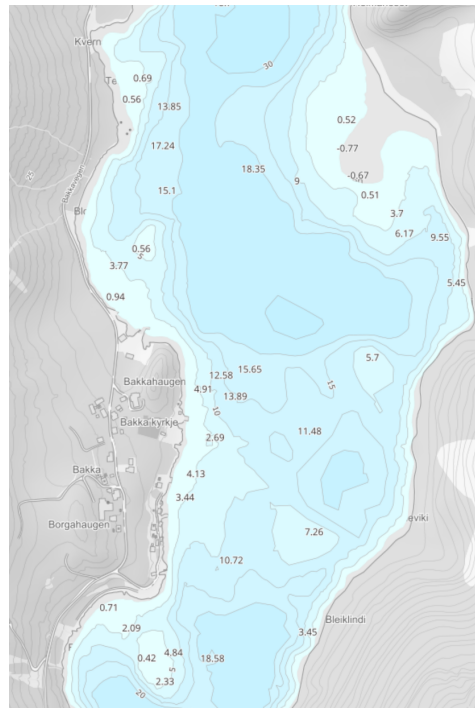
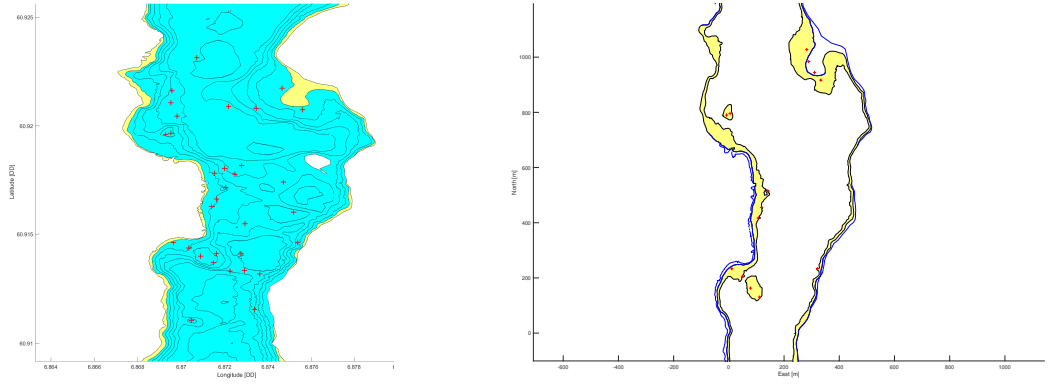


Figure 2.6: Part of the used map as it appears on NMA's online portal. Only the data in Table 2.4 are displayed.

regarding awash rocks, general depth data and shallow areas. These types of data may sound like they overlap, but in some areas of the fjord they did not. The next and third step was to find where in the relevant areas the vessel actually might collide. This was done by looking at the vessels draught multiplied by a small safety factor. After the relevant obstacles are identified, the coordinates of the obstacles are changed from Latitude-Longitude to flat earth North-East coordinates. This was done by a function from Matlabs Aerospace toolbox for simplicity, but the

formulas from Section 2.3 in Fossen (2011) might as well have been used.

Figure 2.7 shows how the computer interprets the map in different processing steps.



(a) The map as it appears after cropping. (b) The map after completed processing.

Figure 2.7: The processing of map data

2.6 Guidance system

2.6.1 The A* path planning algorithm

To control the vessels guidance mechanism, the A* algorithm is chosen. This is a flexible algorithm that is able to construct a path navigating through obstacles, in contrary to a waypoint-based guidance mechanism. This algorithm is a combination of two other algorithms: Dijkstra's and Greedy-Best-First Search (GBFS), and a comparison can be seen in Figure 2.8. Note how GBFS is tricked by the obstacle but explores far less nodes compared to Dijkstra's algorithm which checks more nodes but finds the optimal path. The A* algorithm needs some things to

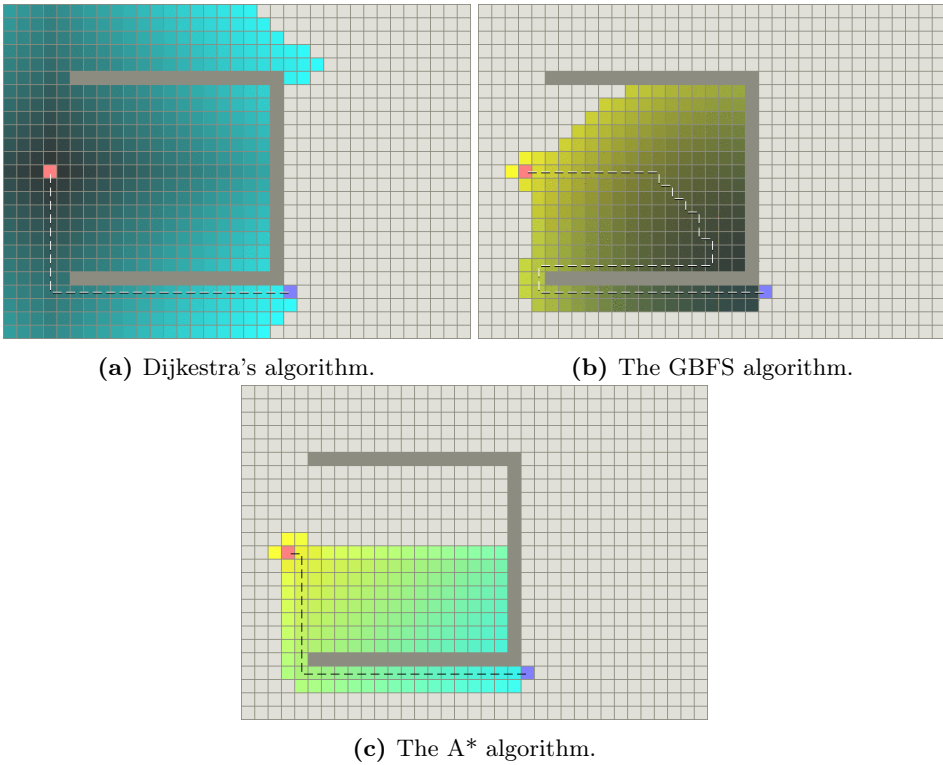


Figure 2.8: Comparison of different path planning algorithms. The coloured area resembles nodes that has been checked, while the stipled lines represent the final path to the goal. Figures retrieved from Patel (2019)

function properly. These are a cost function with a heuristic and a graph. A *graph* is defined as a set of vertices with connecting edges, while a *heuristic* is some kind of estimate of how far a node is from the goal. A heuristic is not necessarily limited to distance, but can also be a measure of any other cost e.g. time or fuel.

A* is based on the following cost function.

$$f(n) = g(n) + h(n) \quad (2.20)$$

where

- n : Current node
- $g(n)$: Movement cost from the starting point to node n when visiting all the other nodes on the path
- $h(n)$: A heuristic - the estimated movement cost from node n to the final destination.

An exact heuristic ensures minimal runtime in addition to a optimal path, or the lowest possible traversed distance. If $h(n)$ is either too small or too big, A* will look more like Dijkstra's algorithm or a greedy-best-first-search, respectively. Also, a heuristic function that never overestimates the cost of reaching the goal node is called admissible. The flow chart of the A* algorithm can be seen in Figure 4.13 A good resource for A* and its implementation can be found in Patel (2019).

Heuristics and tie breakers The heuristic function $h(n)$ is chosen to be the Euclidian distance, as seen in Equation 2.21.

$$h(n) = \sqrt{(n.x - goal.x)^2 + (n.y - goal.y)^2} \quad (2.21)$$

Here, D is a scaling constant with the purpose of giving both $h(n)$ and $g(n)$ the same units. $n.i$ is i -coordinate of node n , while $goal$ is the final destination. This heuristic is chosen because it underestimates the distance unless the goal node(s) is on a obstacle free, straight line from the node n . When the heuristic function is lower or equal to the cost of moving from node n to the goal, A* is guaranteed to find the shortest path. If $h(n)$ is exactly equal to the cost of moving to the goal, then A* will find the optimal path very quickly. In general, the lower the value of $h(n)$, the more time will A* spend. If $h(n)$ on the other hand is greater than the exact distance, A* will run faster but is no longer guaranteed to find the shortest path. If $h(n)$ is much greater than $g(n)$, then A* behaves like Greedy Best-First-Search.

Graphs may have multiple paths that has equal total distance to the goal nodes, which leads to A* spending more time than necessary. To solve this problem one can use *tie breaks*. Important capabilities of a tie-break is to make the $f(n)$ -values different from each other and have a deterministic proposal of the best path. A simple way to break ties is to nudge the scale of $h(n)$. This can be done by Equation (2.22) below.

$$h(n) = h(n) \cdot (1 + p) \quad (2.22)$$

Here, p is a constant factor that should be chosen so that p is lesser than the minimum cost of taking one step divided by the maximum expected path length. The end result is that A* explores far less of the map, but is no longer strictly admissible.

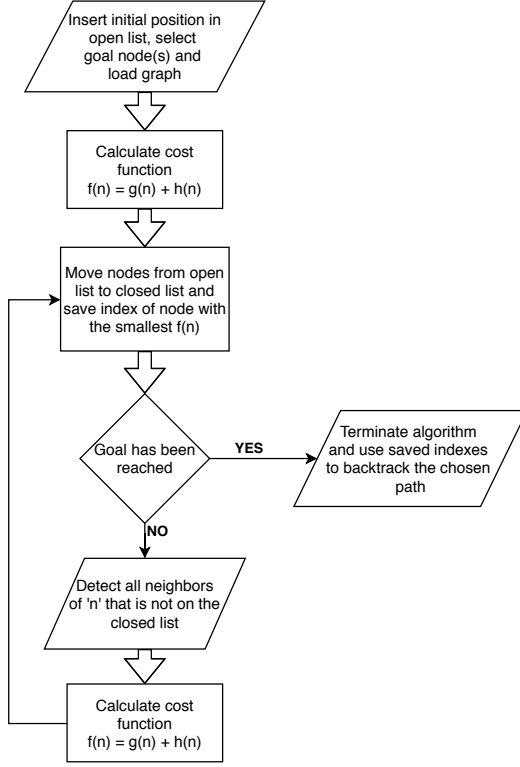


Figure 2.9: Flowchart of the A* algorithm

2.6.2 Line-of-Sight path following

Line-of-Sight (LOS) guidance is a method to generate a desired heading to be used in a heading controller, and thereby force a vehicle to track a path. The method is based on a LOS vector coming out from the vehicle to the next waypoint if it is within the line of sight, or the straight line between two waypoints if not. Figure 2.10 below illustrates the governing principles of the method.

The desired course angle χ_d is calculated from Equation (2.23). Please refer to Figure 2.10a for a better physical understanding of the different symbols.

$$\chi_d(e) = \chi_p + \chi_r(e) \quad (2.23a)$$

$$\chi_p = \alpha_k \quad (2.23b)$$

$$\chi_r(e) := \arctan\left(\frac{-e}{\Delta}\right) \quad (2.23c)$$

$$e(t) = [y(t) - y_k] \cos(\chi_p) - [x(t) - x_k] \sin(\chi_p) \quad (2.23d)$$

$$\Delta(t) = \sqrt{R_{LOS}^2 - e(t)^2} \quad (2.23e)$$

These equations contain a lot of symbols which is in need for some explanation. Starting with Equation 2.23a, this states that the desired heading is the sum of two different angles - the path-tangential angle χ_p and the velocity-path relative angle, χ_r . Physically, χ_p is the angle the vehicle would have if it was positioned on the line between two waypoints while facing the next waypoint. For two waypoints p_k and p_{k+1} , this angle is represented by α_k . The addition of χ_r corrects for the offset in steering angle the vehicle would have when not lying lines between waypoints. As stated by Equation (2.23c), χ_r is defined as the angle spanned out from the LOS vector and the lookahead distance Δ in Figure (2.10b). The lookahead distance Δ represents the line segment between the point of shortest distance between the vehicle and the line, and the intersection of the LOS-circle. Moving on to Equation (2.23d), this defines the crosstrack error e as a function of the vehicles position (x, y) , the position of the most recently passed waypoint (x_k, y_k) and the path-tangential angle χ_p . The lookahead distance Δ is defined by the constant lookahead radius R_{LOS} , as can be seen in Equation (2.23e).

The vehicle needs some switching logic in order to decide what waypoint it is going to search after. This is decided by evaluating if the distance between the vehicle and the next waypoint (x_{k+1}, y_{k+1}) is within R_a , the radius of acceptance. This evaluation is expressed mathematically in Equation (2.24).

$$[x_{k+1} - x(t)]^2 + [y_{k+1} - y(t)]^2 \leq R_a^2 \quad (2.24)$$

For air-and waterborne vehicles transverse forces from the environment can cause the vehicle to drift. To handle this sideslip, the vehicle's desired heading has to be adjusted as seen in Figure 2.10a. This is done according to Equation (2.25).

$$\psi_d = \chi_d - \beta \quad (2.25a)$$

$$\beta = \arcsin\left(\frac{v}{U}\right) \quad (2.25b)$$

Here, ψ_d is the desired heading, β is the sideslip angle, v is the transverse speed of the vessel and U its total speed.

2.7 Bayesian Belief Networks

Bayesian networks (BNs) behaves similar to the human evaluation of probability for something to happen. This comes from the fact that BNs use posterior events to calculate the probability for a new event to occur. For example, a captain on a ship will take the weather and amount manoeuvrable space into consideration when he tries to figure out if he can increase the vessels speed or not.

A core part about BNs is Bayes equation,

$$P(A|B) = \frac{P(B|A)P(A)}{P(B)} \quad (2.26)$$

This equation states the probabilistic relation between two events, A and B. Bayesian networks, which also go by the name belief networks, bayesian belief networks, causal probabilistic networks or causal networks, are *acyclic directed graphs* (see Figure 2.11) BayesFusion (2018). Here, nodes represent random variables and arcs

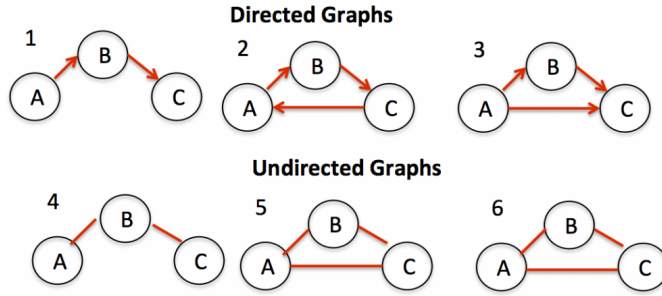


Figure 2.11: Different types of graphs. A directed graph acyclic graph would look like 1 or 3.

represent direct probabilistic dependences among the nodes. Bayesian networks, as graphs, got graphical structure which illustrates the interaction between the variables it models.

Chapter 3

Method

This Chapter presents the used methodology. Figure 3.1 shows an overview of the functionality used in the resulting simulator.

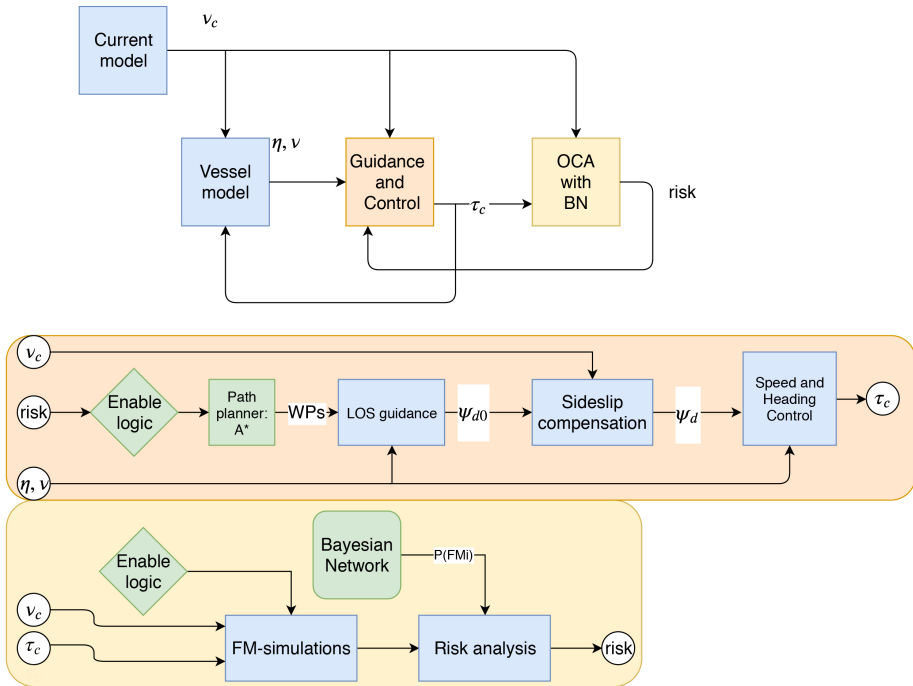


Figure 3.1: Overview over the system used in the thesis. The green blocks has been the focus, while the blue blocks is covered in previous work.

3.1 The OCA simulator

Failure modes The different failure modes (FMs) used in the simulations are defined in Table 3.1. As the propulsion system is not being modelled the speed control is not implemented during the power reducing failure modes. FM0 serves the purpose of finding out what would happen to the vessel if it does not change its course of action.

Failure mode	Probability	Definition
FM ₀	0.50	Simulates the movement of the simplified vessel dynamics ahead for 60 seconds with no errors. Used for control and to replan the path should the simulation end with collision.
FM ₁	0.05	Complete propulsion failure for 40 seconds. The vessel can not produce forward thrust and have lost steering control.
FM ₂	0.07	Thrust reduction by 80% and loss of speed control for 40 seconds before recovering. Modelled by multiplying thrust in surge with 0.2.
FM ₃	0.13	Thrust reduction by 50% and loss of speed control for 40 seconds before recovering. Modelled by multiplying thrust in surge with 0.5.
FM ₄	0.25	Rudder freeze for 40 seconds. Modelled by keeping the vessels yaw moment constant ¹ .

Table 3.1: Used failure modes and their static probabilities when the BN is not in use.

Failure mode dynamics The FM dynamics are based on the linear manoeuvring model presented in Equation (2.14) in Section 2.4.2. The difference is the lack of fluid memory effects. This FM dynamics is being discretized by the discrete version of the combined forward and backward Euler integration, retrieved from Appendix B in Fossen (2011). The discretized linear manoeuvring model is written as

$$\begin{aligned}
 \boldsymbol{\nu}(k+1) = & \boldsymbol{\nu}(k) + h(\mathbf{M}_{RB} + \mathbf{M}_A)^{-1} \cdot ... \\
 & [\mathbf{M}_{RB} \mathbf{U}_r \mathbf{L} \boldsymbol{\nu}(k) + \mathbf{M}_A \mathbf{U}_r \mathbf{L} \boldsymbol{\nu}_r(k) + ... \\
 & \mathbf{D} \boldsymbol{\nu}_r(k) + \mathbf{d}(\boldsymbol{\nu}_r(k)) \boldsymbol{\nu}_r(k) + \mathbf{G} \boldsymbol{\eta}(k) + \boldsymbol{\tau}_{exc}]
 \end{aligned} \tag{3.1a}$$

$$\boldsymbol{\eta}(k+1) = \boldsymbol{\eta}(k) + h[\mathbf{J}_{\Theta}(\boldsymbol{\eta}(k)) \boldsymbol{\nu}(k+1)] \tag{3.1b}$$

In Equation (3.1), k is the current time step and h is the time-step size chosen to be 0.1s, ten times larger compared with the PPM. The force vector $\boldsymbol{\tau}_{exc}$ is defined as

$$\boldsymbol{\tau}_{exc} = \boldsymbol{\tau}_{env} + \boldsymbol{\tau}_c = [\mathbf{X} \mathbf{Y} \mathbf{N}]^\top + [\tau_X \ 0 \ \tau_N]^\top \tag{3.2}$$

where X , Y , N are the nonlinear surge dampening from Equation (2.16) and cross-flow drag from Equation (2.17), respectively. The control force τ_c is made up from Equation(2.19) and Equation (2.18). The control gains of the FM simulations are initiated to the same level as that of the main simulation and is not being individually tuned. Also, due to the high amount of RAM needed to run the simulations, the FMs has a fairly short duration. In order for the vessel to be able to react in case of heightened risk, FM0 runs for 15 seconds before another FM takes over. Due to the potential change in the planned route as a consequence of the delayed start, the time interval between the OCA simulations has been set to 20 seconds in case the new path needs to be updated.

Risk As written in Section 2.3, the risk is defined as the sum of the all the consequence levels achieved during the FM simulations and the corresponding probability for that failure mode to occur. The consequence levels are determined based on the distance to the nearest obstacle and the different threshold used in the simulations can be seen in Table 3.2

Consequence level	CL1	CL2	CL3
Maximum distance from obstacle	45m	15m	5m
Value	0.33	0.66	1

Table 3.2: Consequence levels determined by the distance to the nearest obstacle and thresholds used in the simulations

3.1.1 Bayesian Network

The Bayesian Network (BN) is used to update the probabilities of the different failure modes for the online consequence analysis. For a real vessel this would have to be done by sensor systems measuring the current and other evidence, but for the purpose of showcasing the framework the current velocity (in the body frame) is instead fed right into the BN.

Construction of BN See Figure 3.2 for a display of the used BN used to estimate the probabilities for the different failure modes. Please note that the BN does not serve the purpose of being exact - it only serves the purpose of illustrating the completed framework. The BN contains both dynamic and static nodes, whereof the dynamic nodes are the nodes the ones colored lime green, while the static nodes are the dark green nodes and "Wind evaluation". Here, the dark green nodes are the risk inducing factors identified in Section 2.1. For simplicity, only a few countries, ship types and age groups were used. The probabilities for these dark green nodes are retrieved from Table 5 in Cariou et al. (2008) and a copy can be found in Table A.1 in Appendix A. The node labels "*LesserThan10*", "*LesserThan20*" and "*Lesser than30*" is misleading as the probabilities they represent are $A \leq 10$, $10 < A \leq 20$ and $20 < A \leq 30$, respectively. Another note is that the BN is modelled in such a way that thruster failure and FM4 are not mutually exclusive, while they are mutually exclusive within the FM simulations. The rationale explaining

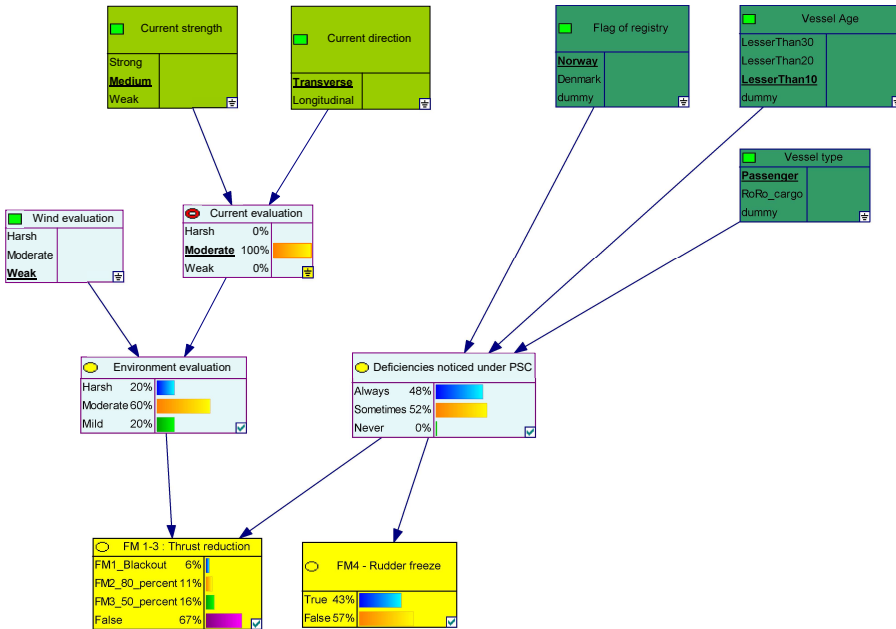


Figure 3.2: Applied Bayesian Network displayed in the GeNie Modeller.

Current strength		Current direction	
'Weak'	$ \nu_c \in [0, 0.5]$	'Transverse'	$\angle \nu_c \in \{(45^\circ, 135^\circ), (225^\circ, 315^\circ)\}$
'Medium'	$ \nu_c \in (0.5, 1.0]$	'Longitudinal'	$\angle \nu_c \in \{(-45^\circ, 45^\circ), [135^\circ, 225^\circ]\}$
'Strong'	$ \nu_c \in [1.0, \infty)$		

Table 3.3: The logic behind setting evidence for the current nodes in the bayesian network

the left side of the BN in Figure 3.2 is that environmental forces causes extra stress on a vessels power system and may therefore be able to cause power failure. The stress might come from high waves causing the fuel pressure in the engine to drop or long periods of high loads.

The joint probability tables within the different blocks has been decided based on the author's best ability. In the case of the node 'Current evaluation' this has been decided by a boolean table where a 'strong' and 'transverse' current is the only combination that can cause a harsh current evaluation. For example, given that the vessel always fails port state controls (PSC's) and that the weather is rough, the vessel has an increased probabilities for all the thrust reducing failure modes. It must be noted that this is not how a BN should be constructed. Ideally one would have statistical data explaining all the different probabilities, but this is rarely the case. Instead, one would have to seek expert opinion and combine this with different methods in order to fill out the joint probability tables. Chapter 8 and 9 in fen is a good resource for such methods.

GeNIe and the connection to Simulink In order to implement the BN into the simulator a software named "GeNIe Modeler" has been used. GeNIe stands for Graphical Network Interface and is a program made by "BayesFusion, LCC", which distribute the program free of charge to academic users.

In order to run GeNIe from Matlab, BayesFusion's SMILE Engine (Structural Modelling, Inference and Learning Engine) wrapper was used. This is GeNIe's application programmer interface (API). SMILE has different kinds of wrappers, but the one used to communicate with Matlab was jSMILE, which is written in the java programming language. In order to run jSMILE a licence is needed. Free 30-day trials and academic 6-month licences can be obtained at <https://download.bayesfusion.com>. BayesFusion also supplies a manual for the SMILE API, BayesFusion (2018), which is available at the same web page.

During the simulation, the evidence for the dynamic nodes is set according to Table 3.3

3.2 Guidance

The guidance functionality in the simulator is combines the OCA framework from Section 2.3 with the A* algorithm from Section 2.6.1 with the LOS path following methodology presented in Section 2.6.2. This is done by feeding the highest measured risk found for all the FMs and evaluating it against a threshold. If the risk passes the threshold, then A* will generate a new path from the vessels current position to the next waypoint. Afterwards, the path will be divided into new waypoints, which the LOS-guidance then uses to steer the vessel.

3.2.1 A* - the path planning algorithm

In order for A* to function properly, it needs some sort of graph. This graph is made by letting a 2D occupancy matrix represent the map area mentioned in Section 2.5. As it can be seen in Figure 3.4a representing the processed map, there are a lot of whitespace between each point. If A* runs on such a grid, the resulting path will just sneak through any non-closed area, which may result in a straight line path. These holes therefore needs to be closed, and this is done by line parameterisation which the following formula describes.

$$L(x, y) := \begin{cases} x = x_1 + (x_2 - x_1) \cdot s \\ y = y_1 + (y_2 - y_1) \cdot s \end{cases} \quad \text{where } s \in [0, 1] \quad (3.3)$$

In this equation, (x_1, y_1) and (x_2, y_2) represents the starting and ending points of the line L. As the A* algorithm allows for diagonal movement, the diagonal gaps has to be closed. This is done by a simple logic first checking if the line the line is straight, and if it is not, setting the adjacent nodes closest to the neighbours to occupied.

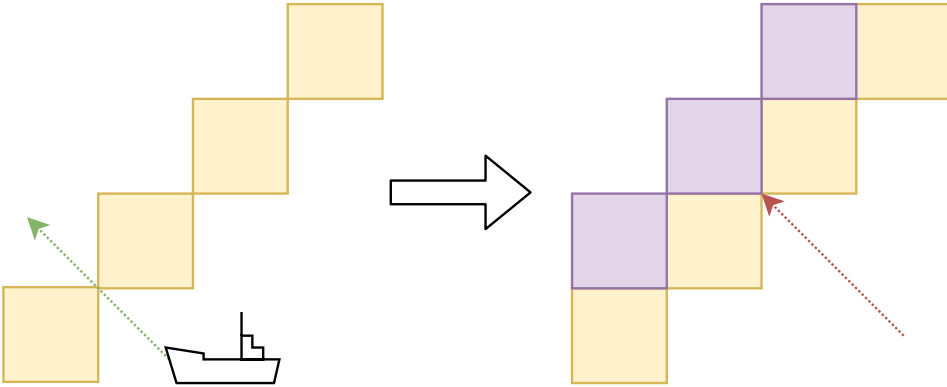


Figure 3.3: Illustration of the process of 'closing' diagonal lines.

In order to improve the runtimes of A* as to make it viable for online execution, A* only runs from position of activation to the next waypoint on the list. This allows for a reduced grid size. The grid size is decided by the starting and ending points and a factor δ , which expands the smaller grid in every direction by a set amount. The δ -factor is used in order to increase the probability that the reduced map is large enough to provide a solution. The factor is based on a percentage increase of largest edge in the rectangle spanned by the starting point and goal which is inputted in the A* algorithm. Note that if δ is too small, this can cause A* to find non-optimal paths. Patel (2019) suggests other methods for reducing the time spent by A* in a particular graph, such as adding hierarchical layers and navigational meshes. These were not implemented due to time constraints.

Next up the risk functionality is added. This is done by imitating terrain, and providing A* with costs for moving in different types of terrain. The terrain type is based on the distance to a obstacle. It is set by iterating through every node in the grid until a obstacle is noticed - then all nodes within a square with the obstacle in its center is set to level 1. The process continues with assigning level 2 and level 3. This process, even though highly inefficient, spends a reasonably low amount of time for a decently large map (ca 1.6 seconds for a grid of 8.11×10^6 nodes). A part of the resulting risk map can be seen in Figure 3.4c. The different terrain costs are incorporated into A* by a change in the movement cost function $g(n)$ in Equation (2.20). This is defined as the following

$$g(n) = D(L)\sqrt{(n.x - N.x)^2 + (n.y - N.y)^2} + \sum_2^{n-2} g(n-1) \quad (3.4)$$

Here, $D(L)$ is a factor used for differentiating the types of terrain from each other.

Terrain type	D(0)	D(1)	D(2)	D(4)
Node distance	d>45m	d≤ 45m	d≤ 15m	d≤ 5m
Cost	1	1.2	2.25	3

Table 3.4: Movement costs in different types of terrain in A*.

After the path has been generated waypoints are to be generated. This is done by first transforming the path coordinates from the reduced grid to the global grid and then secondly to make waypoints out of the path. Third, the new list of waypoints are combined with the old list of waypoints. In order to transform the coordinates over to global coordinates the following formula was used.

$$P^{global} = P^{local} - P(1)^{local} + P(1)^{global} \quad (3.5)$$

Here, P is a row in the waypoint matrix $n \times 2$ matrix whereof each row inhabits the NED coordinates of each step in the path, ordered from the starting position ($P(1)$) to the ending position ($P(n)$).

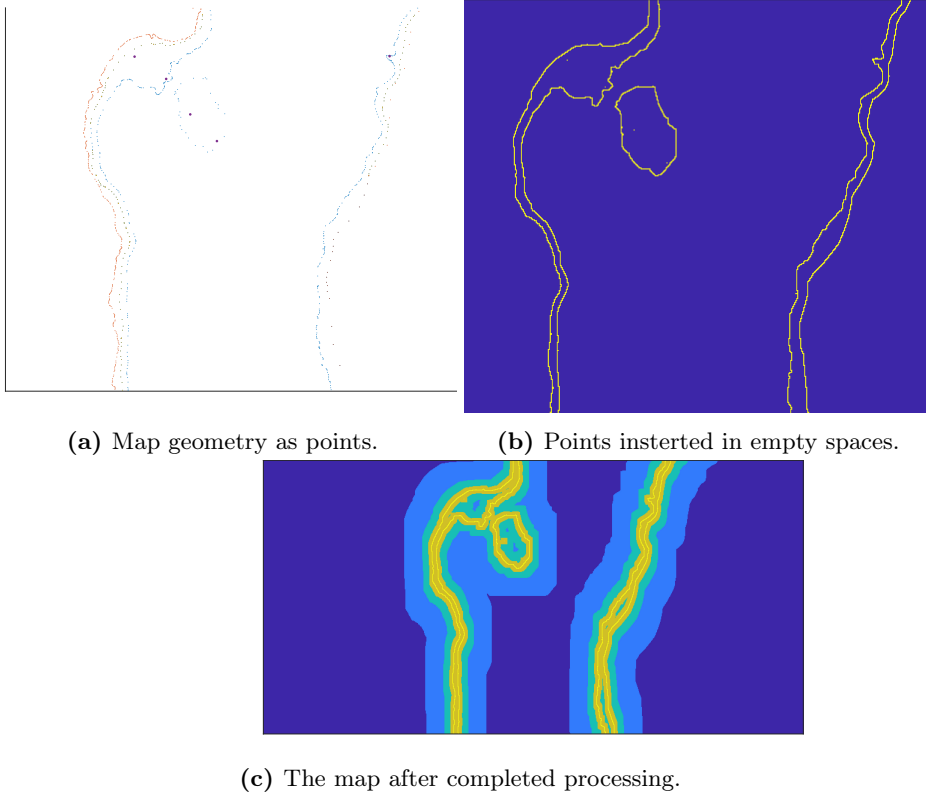


Figure 3.4: Gradual processing of the A* grid, from separate points in (a) to connected points in (b) and finally the complete risk map in (c)

The generation of waypoints from the A* path is done by evaluating which path coordinates that lies between two straight lines and make waypoints out of the coordinates that does not fall between the two lines. Mathematically, the criteria of evaluation can be stated as

$$y_a \leq y \leq y_b \quad (3.6)$$

where y is the line between two waypoints, $y_a = y - \delta$ and $y_b = y + \delta$ and where δ is the distance from the middle line. The reason for reducing waypoints is to make the waypoint queue less cluttered, and to make it easier for the waypoint shuffler to insert new waypoints at the correct location in the queue.

Chapter 4

Results

4.1 Validation

4.1.1 Vessel model and environment

Figure 4.1 aims to showcase how the the simulation model consisting of the vessel dynamics presented in Section 2.4.2, the control theory presented in Section 2.4.3 and the LOS path following from Section 2.6.2 works for both the process plant and the failure mode dynamics. The Figure show the vessel starting in WP1 and navigating to waypoint four, while being affected by a current flowing from west to east with a speed of $1.5 \frac{m}{s}$. The failure mode simulation starts after 15 seconds and the LOS radius of acceptance has been set to 2x length between perpendiculars (Lpp). From Figure 4.1 it can be seen that the simulated vessel drifts east at the start of the simulation. This is due to the current and is expected. The failure mode simulation starting at the blue rectangle behaves exactly like the main simulation until it is within the radius of acceptance of WP2. At the point of turning to WP3 it can be observed that the FM simulation has a greater curvature than the main simulation. This is also the case during the next turn, from WP3 to WP4. One can also notice that both simulations seem to converge to the same position in both WP3 and WP4, albeit with a different heading. Ideally the failure mode simulation should, when no failures are present, replicate the main simulation with high precision. Also, the simulated trajectories after the blue triangle are not optimal in terms of going the shortest path. This is likely due to poor tuning of the heading autopilot. The main takeaway from Figure 4.1 is that there is a considerable discrepancy between the main simulation and the failure mode simulation for non-straight paths.

To better examine the differences between the two models, Figure 4.2, Figure 4.4 and Figure 4.3 has been produced. These figures compares the relevant states for the main simulation and failure mode simulation after the blue rectangle mark in Figure 4.1. In these figures, Δ is defined as the value of a state within main simulation subtracted the value of the failure mode simulation.

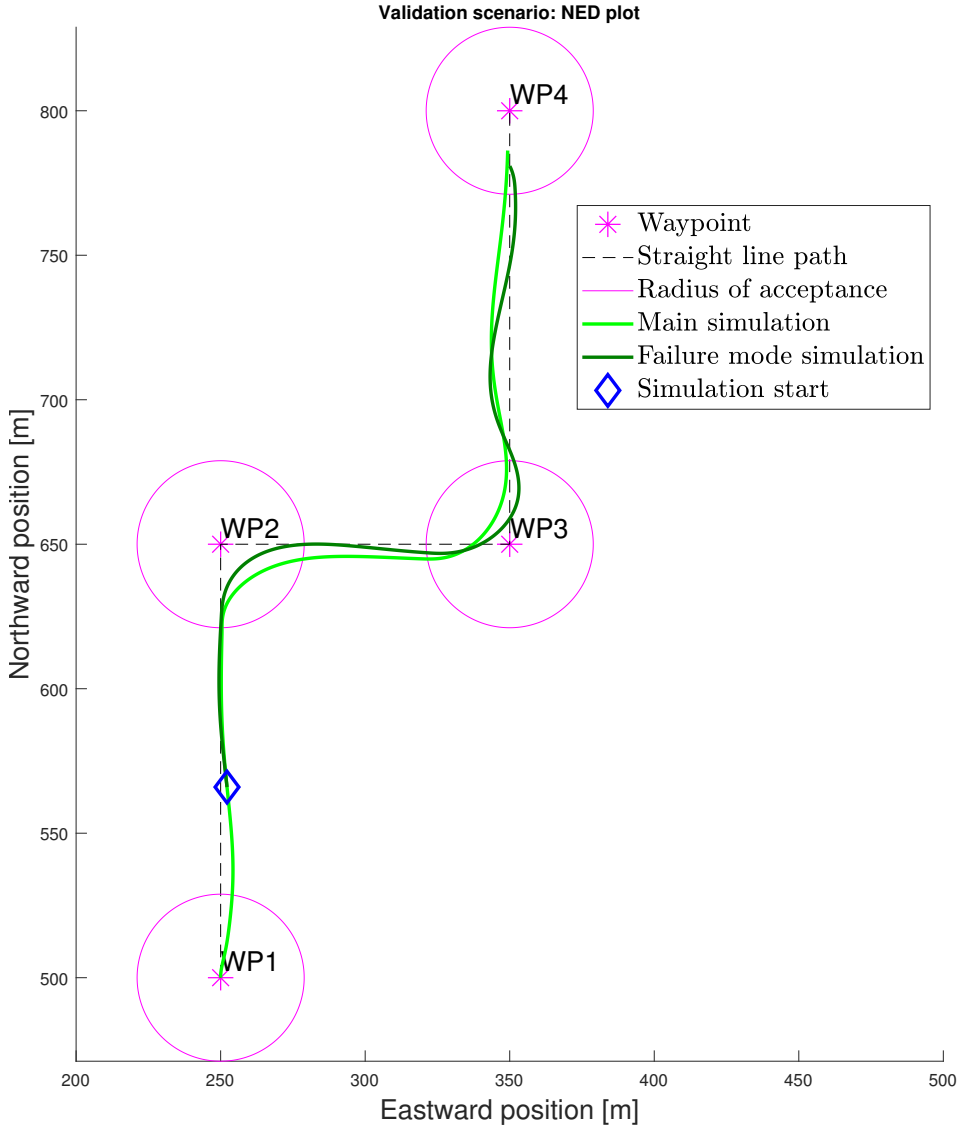


Figure 4.1: Comparison between simplified model and simulation model navigating through waypoints under the influence of a eastward current.

Figure 4.2 displays the North and East-coordinate produced by the two simulations as a function of time. By looking at the red error curve, it can be seen that the north position in the failure mode simulation (N_{fm}) lies on or above the north position for the main simulation (N_{main}) until $t \approx 30$ s. Afterwards, N_{main} is above N_{fm} . This happens a bit after the simulations reach the radius of acceptance of

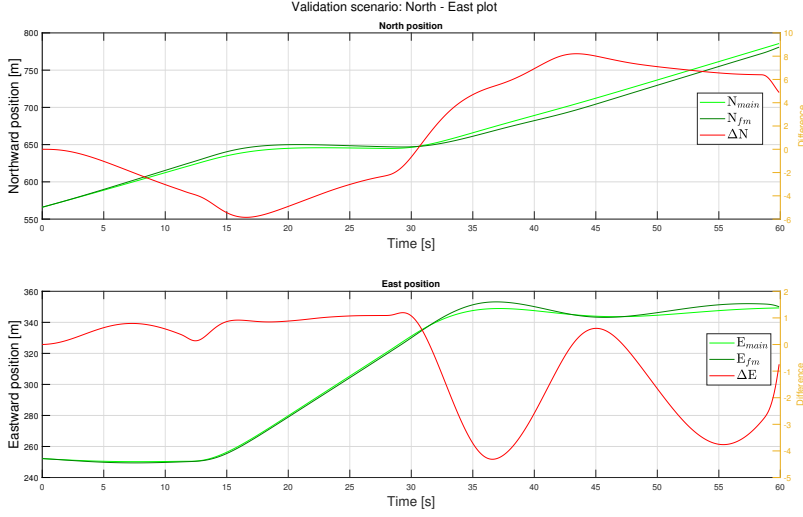


Figure 4.2: Northward and eastward position for the main simulation and the failure mode simulation in the validation scenario presented in Figure 4.1.

WP3. It can also be seen that the discrepancy ΔN are in the range $[5.8, +8.2]$. The two simulations are more aligned for the eastward position as can be seen on the bottom graph of Figure 4.2. Here, the discrepancy ΔE is in the range $[-4.3, +1.2]$ and occurs during the turn from WP3 to WP4. Combined, the northward and eastward plots in Figure 4.2 suggest a discrepancy in forward speed and turning rate. This is plotted in Figure 4.3. In Figure 4.3 one can easily observe the two curves representing the simulations do not follow each other very well. This is especially the case for surge speed, or the ships forward motion. However, the numerical difference is not that large with a peak of $+1.2$ and trough of -0.5 . There can be several reasons for this. First, the simplified dynamics in the failure mode simulations do not account for fluid memory effects and its differential equation time step size is ten times larger. The different behavior at the end of the simulation is expected as the failure mode simulation do not have any exit logic when the final waypoint is reached.

Lastly, the heading and yaw rate graphs for the failure mode simulation and the main simulation is presented in Figure 4.4. In Figure 4.4 one can observe that the heading is mostly equal for the two simulations up until t_{28} . At this point in time the main simulation turns earlier than the failure mode simulation.

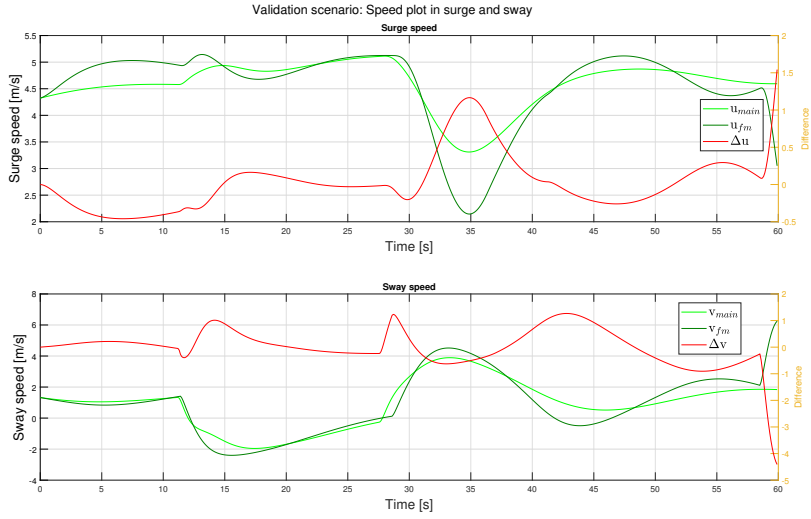


Figure 4.3: Speed in surge and sway for the main simulation and the failure mode simulation in the validation scenario presented in Figure 4.1.

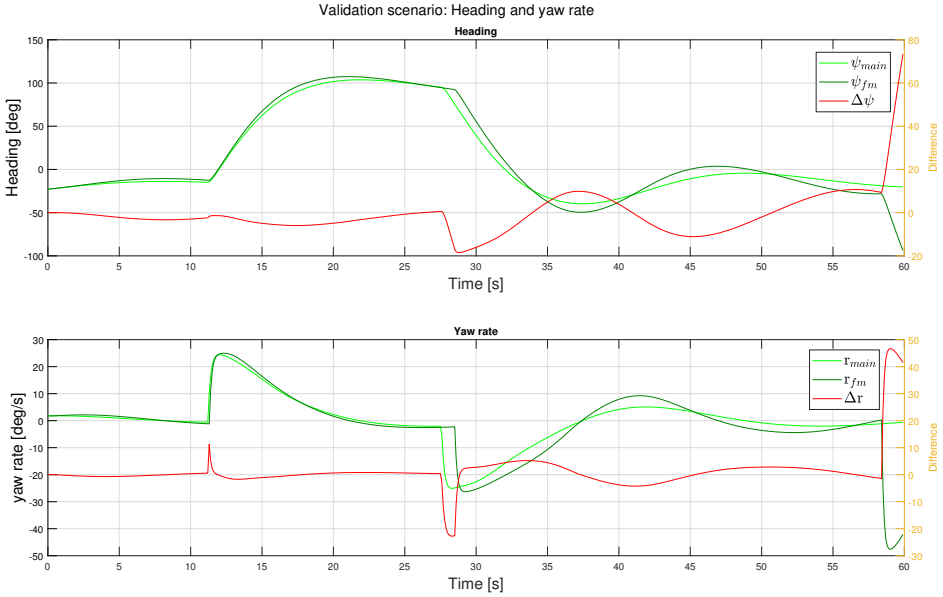


Figure 4.4: Heading and yaw rate for the main simulation and the failure mode simulation in the validation scenario presented in Figure 4.1.

4.1.2 OCA

In order to verify that the different failure modes simulate realistic behaviour, Figure 4.5 to Figure 4.8 are presented. These display the FM dynamics laid forth in Section 3.1 applied to the map presented in Section 2.5. In these simulations, the failure mode will not kick in before 15 seconds into the actual simulation in order to easier validate the different failure modes up against the "no failure" mode. Also, the time interval from the end of one simulation to the start of the next simulation has also been set to 15 seconds. Ideally, this would make the start of simulation n overlap with the activation of the failure mode in simulation n-1. The waypoints are the same as in Figure 4.1 in order to keep the focus on the failure mode simulations. As in the simulation showcased in Figure 4.1, the current has been set to $1.5 \frac{m}{s}$ flowing east.

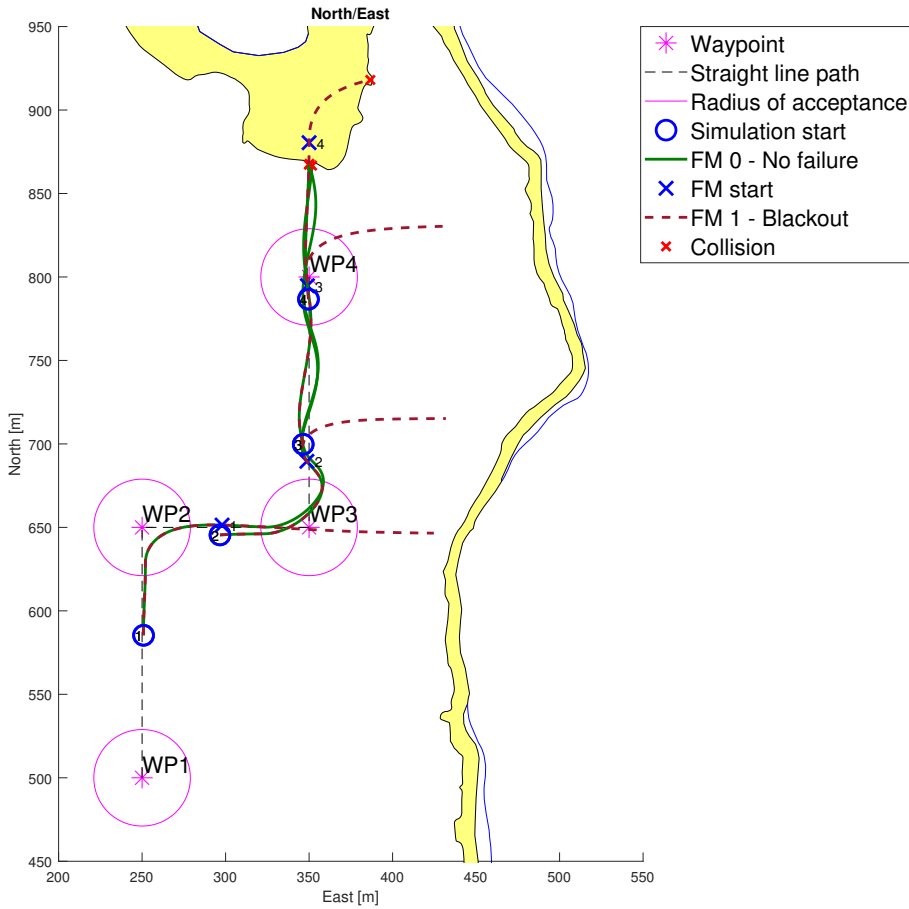


Figure 4.5: Validation: simulations of FM 1.

Figure 4.5 showcases FM 4 - total blackout. The failure mode works as expected: it follows the green "no failure" line up until the failure mode activates, before the vessel starts to drift in the direction of the current. What is more notable is that collision is not registered for the last simulation. This is alarming, as it makes it possible that the associated CL might not be correctly assigned due to the fact that both collision and CLs are based on the distance to the nearest obstacle. Also, a lack of overlap of the green curves can be observed. The lack of overlap is due to the discrepancy between the main simulation and the failure mode simulation as showcased in Section 4.1.1. In tight areas this can result in different CLs being assigned.

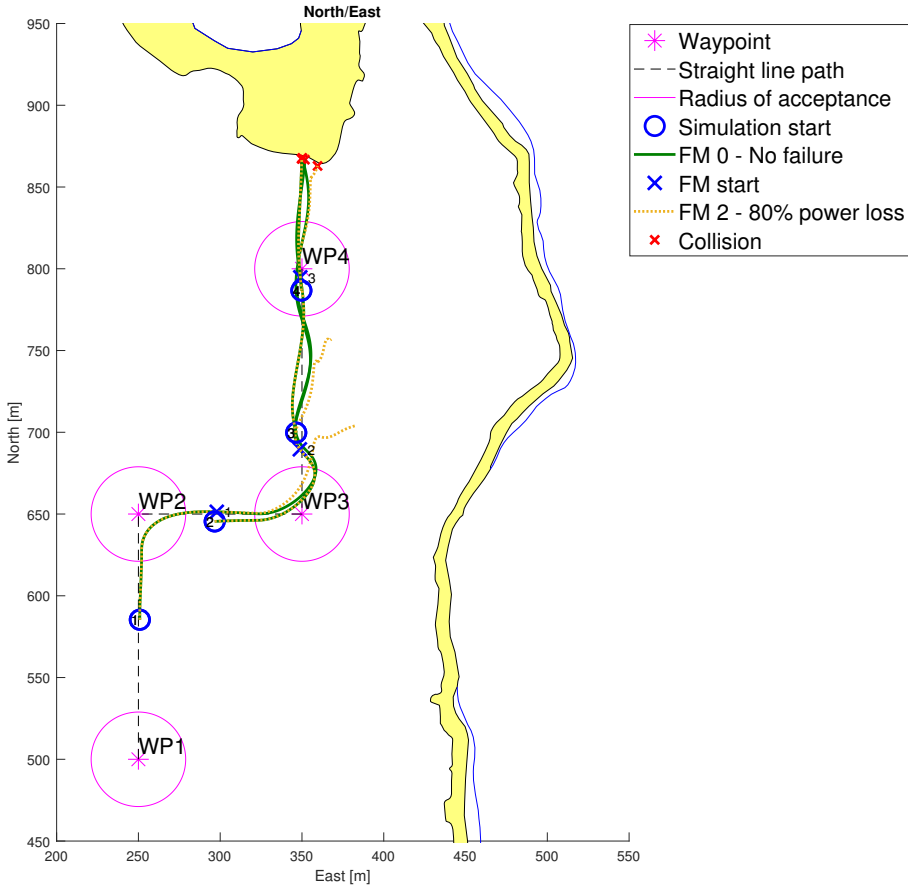


Figure 4.6: Validation: simulations of FM 2

In Figure 4.6, the dynamics representing a 80% power loss is being displayed. It can be observed that the different simulations acts differently. This is a result of the definition of the failure mode: holding 20% of the commanded thrust during the duration of the failure mode. This implies that the different simulations most

likely keeps a different thrust, and therefore reacts differently. Yet, some strange behaviour can be seen at the very end of the the first and second simulation of FM2.

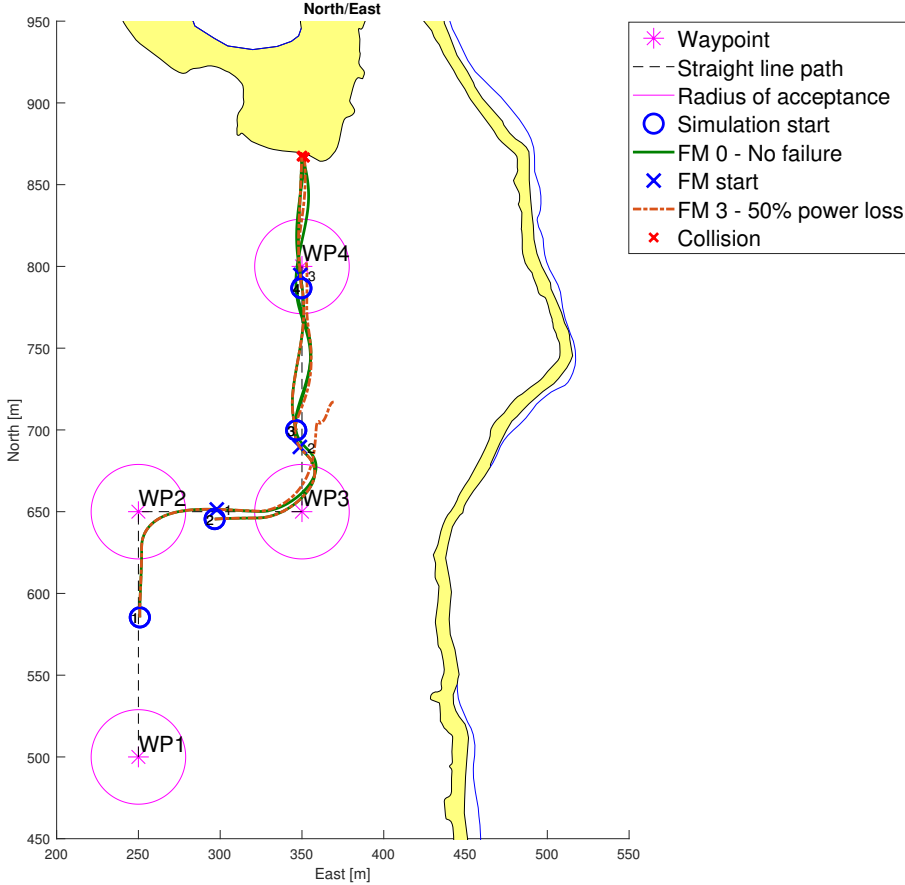


Figure 4.7: Validation: simulations of FM 3.

In Figure 4.7, FM 3 corresponding to 50% power loss is being showcased. As expected, FM 3 behaves more similarly to FM 0 than FM 2 did in Figure 4.6. It can be seen simulation 1 struggles with keeping the path above WP 3, which is explained by the low thrust commanded by the control system at X1 when the vessel is travelling in the direction of the current.

Lastly, Figure 4.8 shows the trajectories generated by FM 4 - rudder freeze. When keeping in mind the eastward current and that the failure mode is defined by keeping the commanded yaw moment constant, there are no surprises when watching Figure 4.8. Unfortunately, collision should have been detected for the third simulation (curved line above WP4).

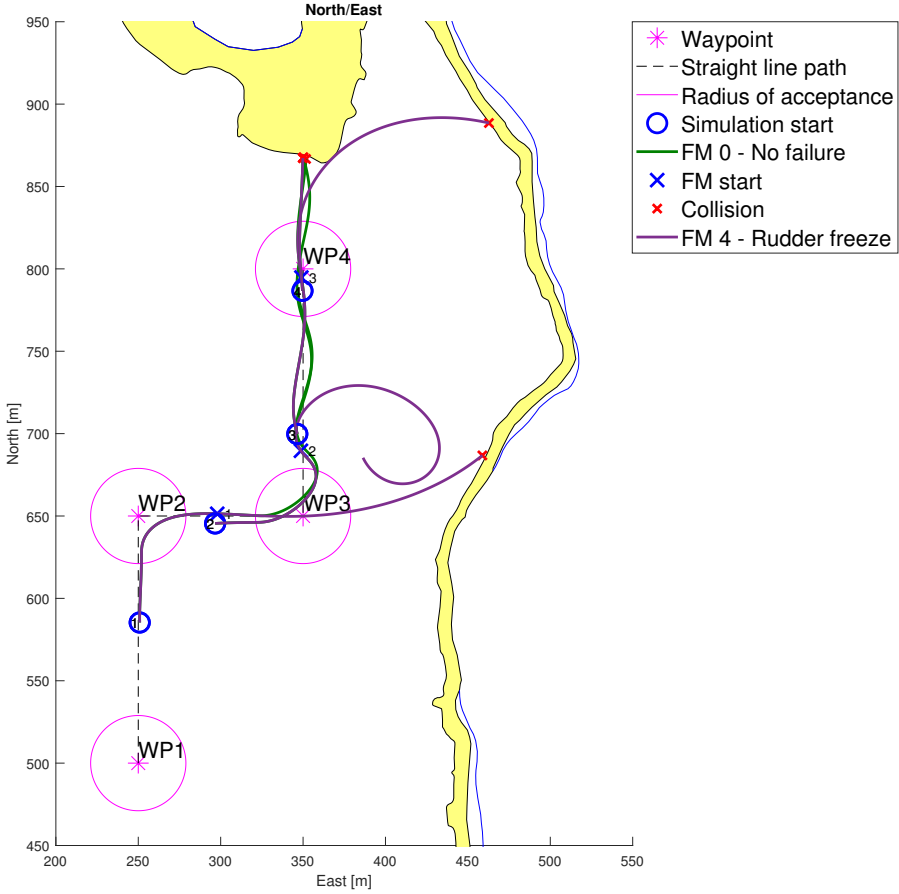


Figure 4.8: Validation: simulations of FM 4.

Figure 4.9 displays the highest CL achieved during the different failure mode simulations showcased in Figure 4.5 to Figure 4.8. For graph readability, the CL has been set to -1 for simulations that otherwise would have stayed at zero. As there is no logic for stopping a failure mode simulation after the last waypoint has been reached, several failure mode simulations end with collision after passing WP 4. This is especially the case for FM 0, as each trajectory travels a longer distance due to a higher forward speed making all simulations except the first result in a collision above WP 4. Looking at FM 1, all simulations show a positive CL. Keeping in mind the CL ranges presented in Table 3.2, a comparison with Figure 4.5 verifies the obtained CLs. FM 2-4 do not show any surprises either.

In order to get an image of how the perceived risk develops with time during the vessels path during the simulation in Figure 4.1, Figure 4.10 has been produced.

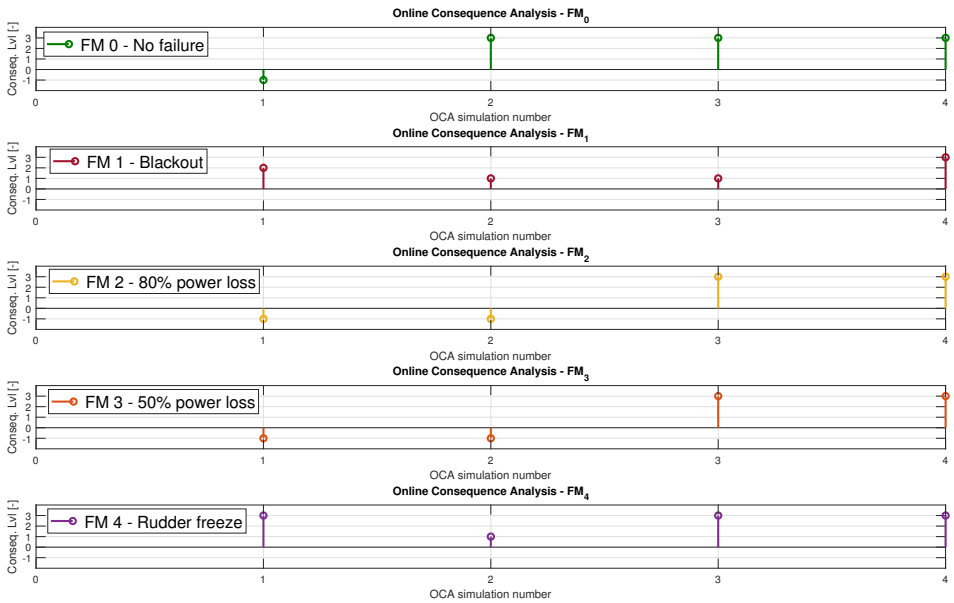


Figure 4.9: Validation: resulting consequence levels for the different failure modes.

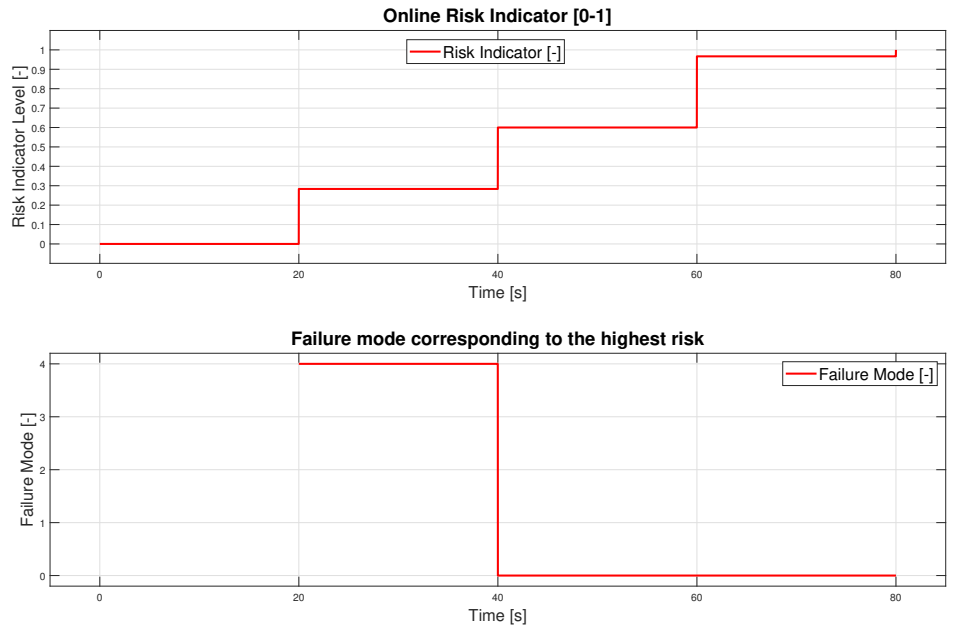


Figure 4.10: Changes in risk and most important failure mode for the simulation in Figure 4.1.

It can be observed that the risk rises steadily from zero, as no OCA simulation has been initiated, and peaks in the last time step. Taking Figure 4.9 into consideration, this is not a surprise as more and more simulations result in collisions. The bottom plot in Figure 4.10 shows which failure mode that is responsible for the highest risk for each time step, and this also fits well with Figure 4.9.

4.1.3 Bayesian network

In order to test the bayesian network (BN), the simulation displayed in Figure 4.1 is run with and without a change in the currents strength and direction. As the risk is only a function of the probability for a given failure modes times the achieved consequence level and the consequence level do not change given that the path is the same. It is therefore sufficient to show that only the probabilities change in a reasonable manner in order to show that the BN works as intended. The BN's static evidence is in listed Table 4.1.

Node	Assigned evidence
Wind evaluation	'Weak'
Flag of Registry	'Norway'
Vessel Age	'LesserThan10'
Vessel type	'Passenger'

Table 4.1: The Bayesian network's static evidence for different nodes.

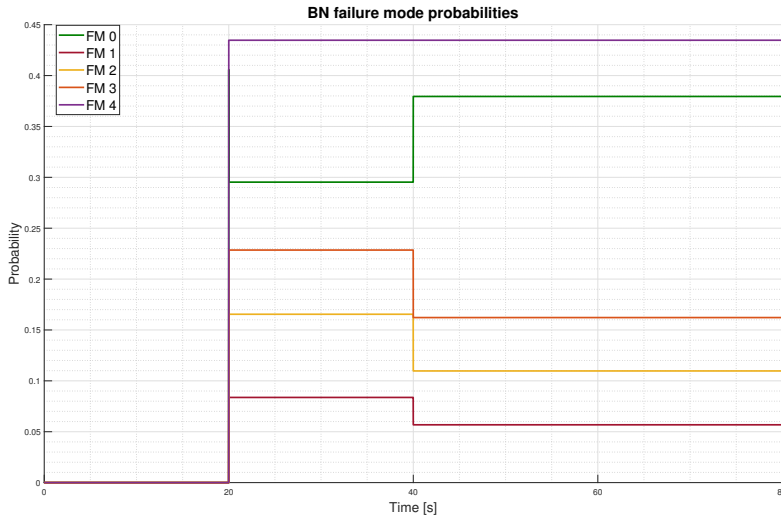


Figure 4.11: Probabilities for different failure modes with constant current.

Figure 4.11 shows that every probability except that of FM 4 changes as the vessel follows its route. This is expected, as FM 4 only is dependant on the static nodes as shown in Figure 3.2 in Section 3.1.1. One can also note that the probabilities only change on the discrete timestamps $T=20$, $T=40$ and $T=80$. This is because the BN is only evaluated when the OCA is initiated. By comparing with Figure 4.5 and Figure 4.4 at $T=20$ and $T=40$ (marked by the first and second blue circle in Figure 4.5) one can observe that the current starts as transversal and then becomes

longitudinal at $T=40$. At $T=60$ the current should be transversal again, though this does not seem to be the case. This could be explained by the sideslip compensation causing the vessel to travel with an angle which according to Figure 4.4 is approximately -25° . This does however not put the current angle in the 'longitudinal' range.

By changing the current strength from $1.5 \frac{m}{s}$ to $0.40 \frac{m}{s}$ flowing southwards, and thereby setting the evidence for the node 'current strength' from 'strong' to 'weak', the following result in Figure 4.12 was achieved. Here it can be seen that the

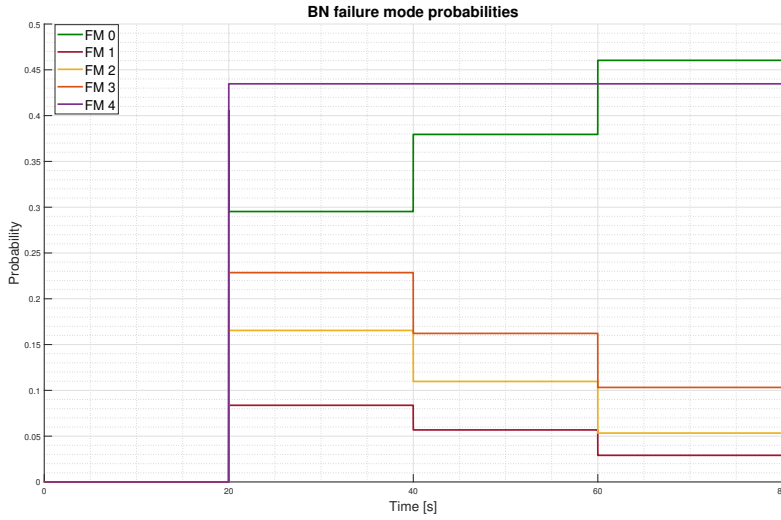
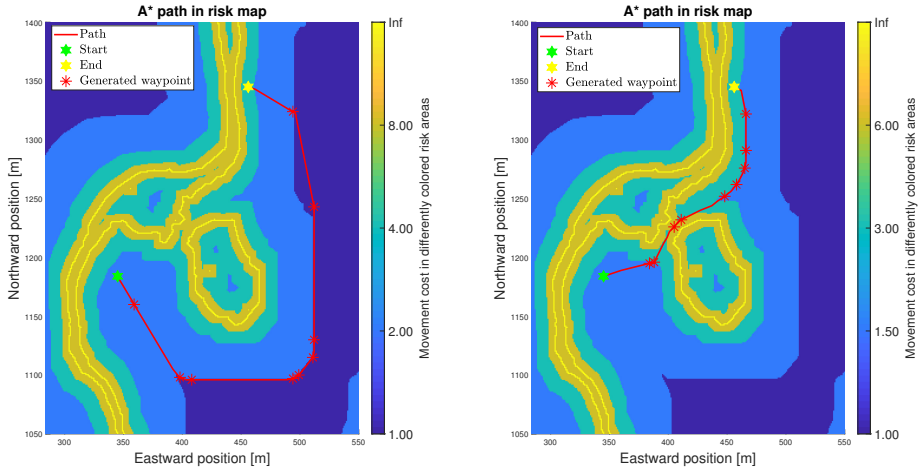


Figure 4.12: Probability for different failure modes with varying current.

probability for FM 1-3 clearly drops several times, as one would expect.

4.1.4 A*

Figure 4.13b and Figure 4.13a showcases the performance of the A*-algorithm with implemented risk terrain and waypoint generation. As expected, the different paths vary with the movement cost of the different risk areas. It can also be seen that



(a) High movement cost of risk.

(b) Low movement cost of risk.

Figure 4.13: A* paths with different movement costs.

the waypoints are placed at the end of seemingly straight lines, as intended.

4.2 Combining the parts

When combining all of the above features with the simulation parameters in Table 4.2 we get the results showed below in Figure 4.14 to Figure 4.17. Due to the vessel navigating through narrow passages, the radius of acceptance had to be reduced.

CL distance zones	[60 15 5]
Movement cost for CL 1-3	[3 6 9]
Enabling risk threshold	0.5
OCA frequency	1/20s
Current strength and direction at T=0s	$0.5 \frac{m}{s}$, -90°
Current strength and direction from T=120s	$1.5 \frac{m}{s}$, 90°
LOS radius of acceptance	$L_{pp}/3$

Table 4.2: Simulation parameters

Figure 4.14 8 waypoints has been selected. The vessel then travels from waypoint to waypoint. One can notice that the pathing has changed by a fair lot, tending to choose areas further away from land due to the lower movement cost. This is due to the generated waypoints following an increased risk from an OCA simulation which is why there are so many generated WPs between WP2 and WP4. After WP4 there is a stretch with no WPs at all, due the risk not exceeding the threshold. This comes from the low probability for the failure modes due to the low current velocity.

In order to take a closer look on the difference in pathing between the ordinary LOS guidance and the new framework, Figure 4.15 and Figure 4.16 are presented. In Figure 4.15 the difference is rather small before WP3. However, as soon as the area with low depth is passed the vessel seeks towards deeper waters. In Figure 4.16 one can notice that the vessel tries to keep the distance to shallow areas as long as possible. One can also notice that due to the higher density of WPs the vessel enters the narrow area between the isle and land with a better angle, which enables the vessel to get a better distance from the isle. Without the added framework the vessel collides at the isle.

Figure 4.17 compares the level of risk for the vessel with and without the new functionality as the vessel follows its trajectory and displays which failure mode that is responsible for the highest amount of risk. It can be seen from the top plot that the level of risk for the new framework is noticeably lower compared to the old for a total of 80 seconds and higher for a total of 60 seconds when completing the horizontal line for the old framework to T=260s. For the bottom plot both frameworks deem "FM0 - no error" and "FM4 - rudder freeze" the most risky, but at different times. Overall, the new frameworks deems FM 4 more risky than plain LOS steering.

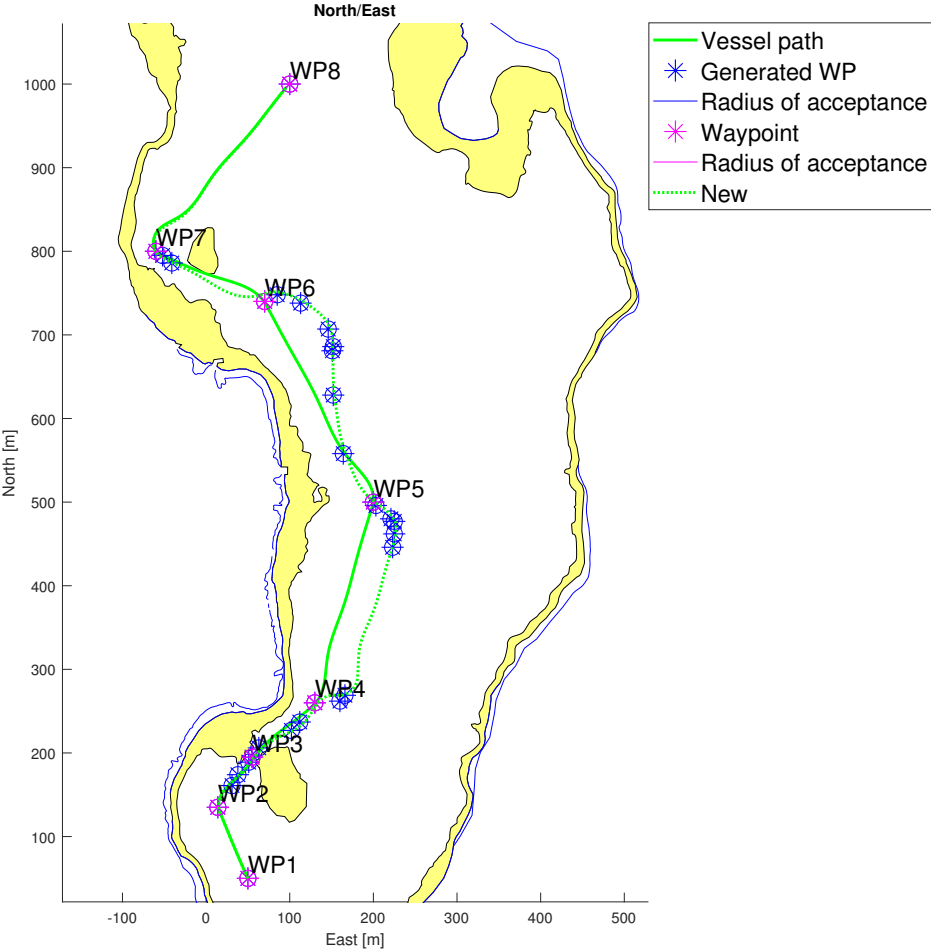


Figure 4.14: NED plot of simulation with A* and BN boosted OCA.

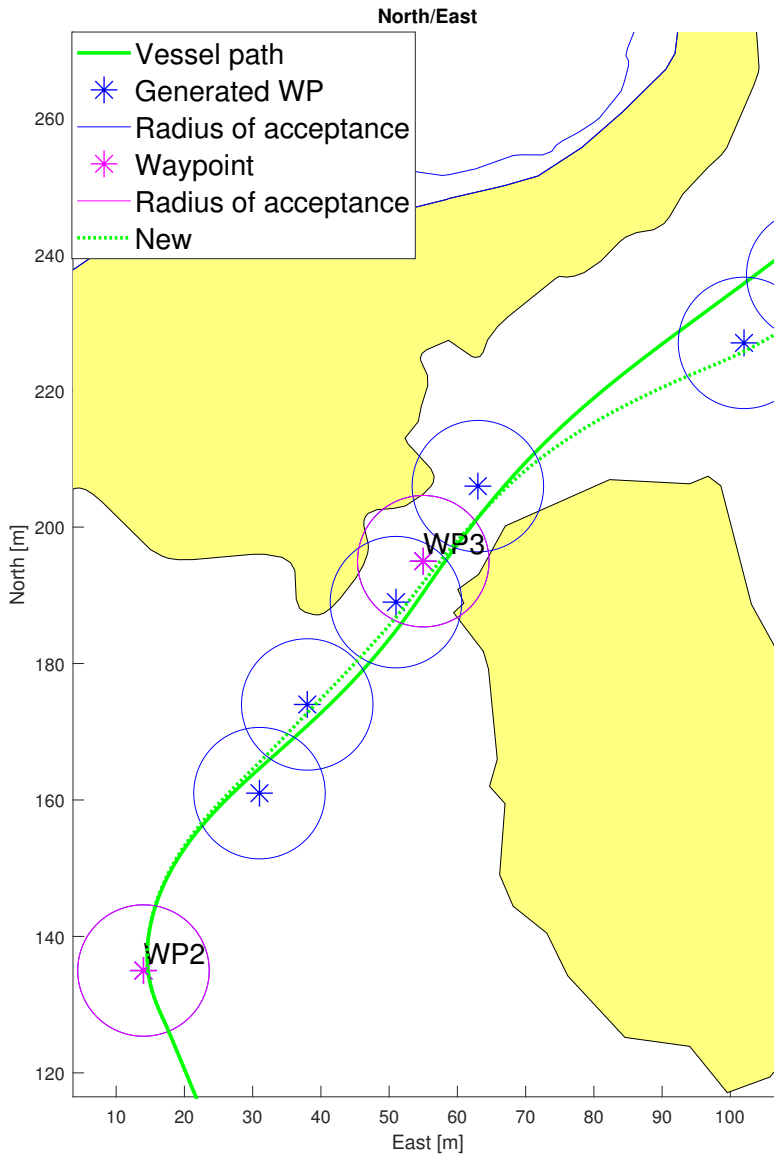


Figure 4.15: Zoomed NED plot of simulation with A and BN boosted OCA showing different pathing.

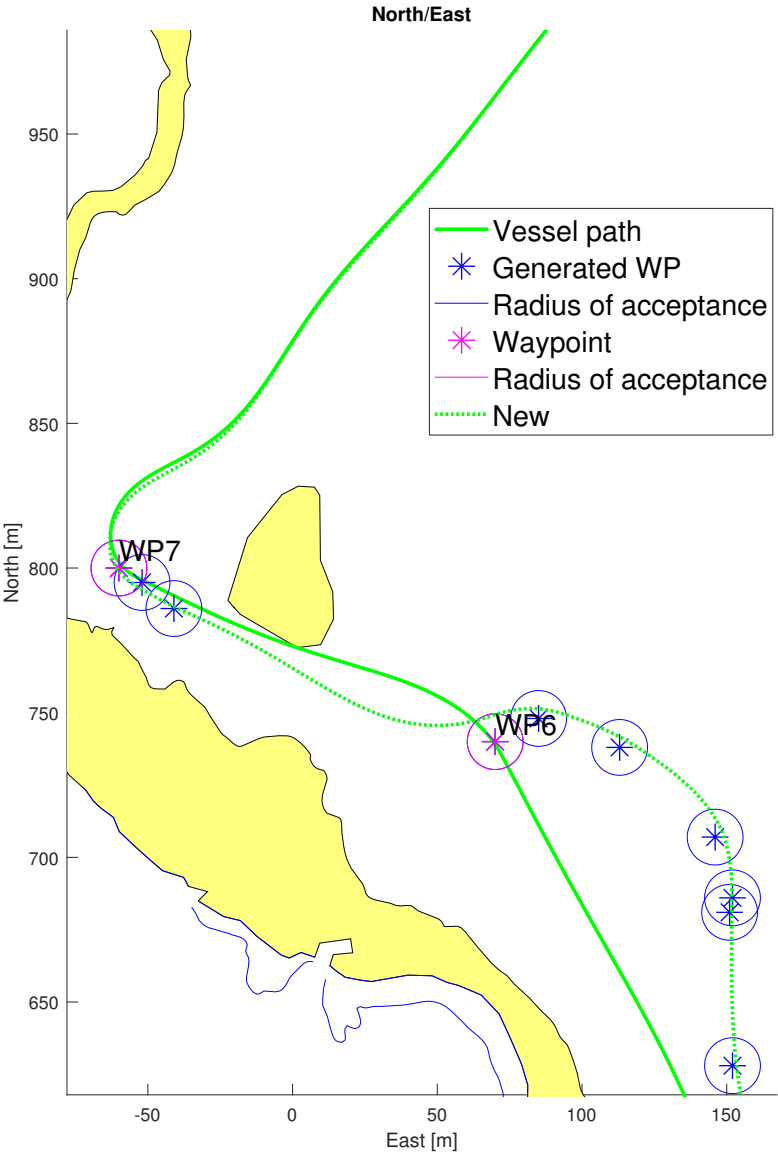


Figure 4.16: Another zoomed NED plot of simulation with A and BN boosted OCA showing difference pathing.

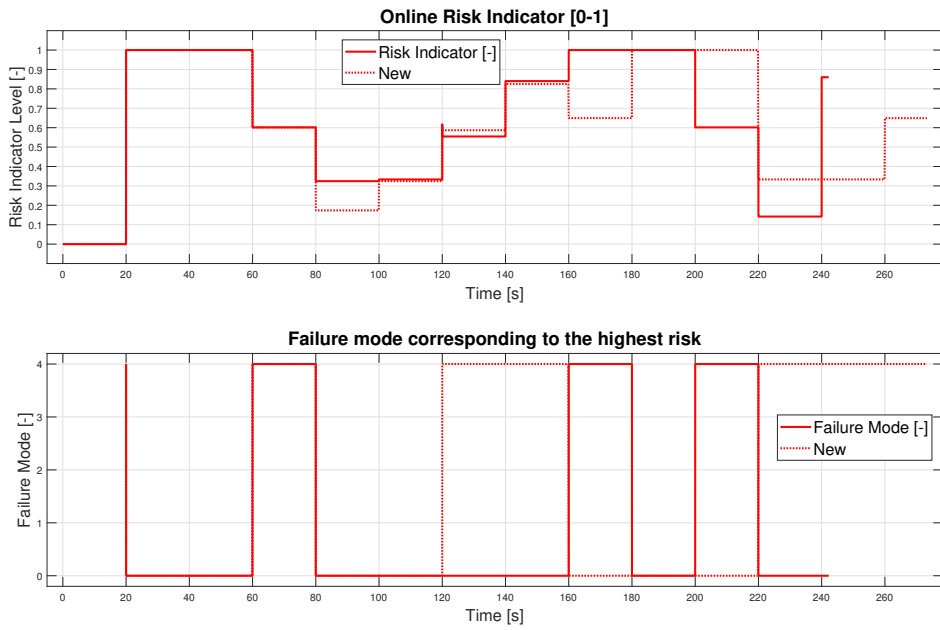


Figure 4.17: Comparison of the perceived risk for the simulation in Figure 4.14 and the failure mode contributing to the highest amount of risk.

Chapter 5

Discussion

Validation The used simulation model, or process plant, seem to display the vessel dynamics in a realistic manner. The simplified vessel dynamics used for the Failure Mode (FM) simulations in the Online Consequence Analysis (OCA) emulates the process plant fairly well but is hindered by the lack of tuning for the speed control. This tuning can be difficult without a thruster model setting a limit for requested force output, as the simplified FM simulations lack the extra resistance that comes from fluid memory effects. The consequence of an unaccurate FM simulation model can potentially give a large increase in risk, especially when the risk is a function of the distance based consequence levels.

The different failure modes simulate their job well, with the exception of FM2 and FM3 showing some strange behaviour at the end of their paths. The reason for this is unknown.

The probabilities outputted from the Bayesian Network (BN) are far away from being realistic but they serve their purpose of giving sizeable changes in risk. In order to find out whether there is a bug in the code or in the network, the angle of current in the body frame should be plotted and read at the relevant time stamps. Even though there might be a minor error in the BN it and its integration into the rest of the model serves its purpose as it updates the probabilities for failure modes given input from the simulated environment.

The modified A* algorithm works seemingly without errors. It and its integration provides waypoints for the LOS guidance to follow, and it is able to avoid areas with high cost. However, the risk is integrated badly into the planning of the path as it does not change the movement cost of crossing different areas in the risk map. Hence the only connection between the path planning algorithm and the risk metric is that the risk zones in the risk map uses the same distances as consequence levels in the risk analysis. As seen in Figure 4.14 this has some effect on the perceived risk due to the vessel wanting get some distance from the risky area. With the current framework, a meaningful connection between the risk metric and the risk-grid movement costs should be easy to implement.

Performance As briefly mentioned in the last paragraph, the vessel model with integrated OCA, BN and a modified A* path finding algorithm works, but only performs marginally better in terms of risk level compared to ordinary LOS guidance. This is in spite of the distance from obstacles is increased for most of the time and collision is avoided, as can be seen in Figure 4.14. The reason for this is the nature of the FM simulations, which can behave rather randomly based on the circumstances in the time of initiation. From the results in the last chapter, it does seem to find more optimal pathing in terms of leaving the risky areas faster, but this is at the cost of an increased travel distance. Both of these properties can easily be changed by tuning the consequence level distances responsible for the risk and the cost of risk within A*. Another option is to make the risk ranges used in A* a multiple of the CL ranges to provoke more risk restrictive behaviour.

Main outcome The main outcome of the work is the integration of Online Consequence Analysis (OCA), a Bayesian Network and a modified A* path planning algorithm into a vessel simulator. The path planner activates when a certain risk level is reached and proposes new paths, as can be seen in Figure 4.14. The integration of Online Consequence Analysis (OCA), a Bayesian Network (BN) and the A* path planning algorithm was successful in the purpose of lowering the chosen metric for risk by a small amount during simulation. By comparing the different paths chosen by the framework and ordinary LOS guidance one can observe that the framework is able to avoid collision, while ordinary LOS is not and that the overall path seems much safer even though this does not show in the risk measure. This is due to the nature of the chosen failure modes. However the connection between the path planner and the measure of risk is thin, due to the fact that the movement costs used by the planner are only implicitly connected with the risk. The connection is based on applying the same distance zones defining the Consequence Levels (CLs) in the OCA as the risk terrain in the A* algorithm. Consequently, the path planner will always avoid those areas, even when the risk is low. The vital connection between the risk movement cost and risk is missing.

5.1 Further work

As mentioned in the last section, the A* algorithm cost of risk should be dependant on the measured risk. This would result in smarter paths suggestions given that the measure of risk is good. In order to make the framework account for the discrepancy between the actual vessel and the FM simulations, a range of motion could be computed. A simple and computationally inexpensive method that would be to add and subtract a fixed amount of distance to the trajectory from a FM simulation, as illustrated in Figure 5.1. The framework presented in this thesis operates with a constant radius of acceptance within the LOS guidance system

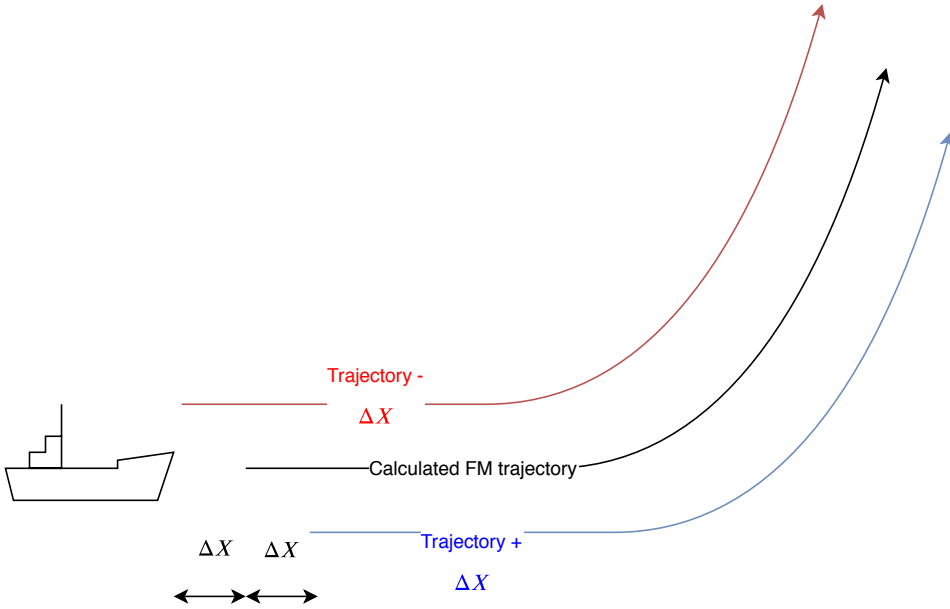


Figure 5.1: Method for handling inaccuracy in the simplified simulation model

presented in Section 2.6.2. An improvement would be to be able to relax this radius when the risk is low and the waters are clear, and to tighten it when the risk grows. This allows for more precise control during periods of high risk which in turn allows the vessel reduce the risk by sticking to the assigned path. One could also make a reference model for the vessels speed that is risk dependant, i.e. the vessel slows down when the risk is high. The measure of risk should incorporate the time spent needed to cross the different CLs as it takes longer time there is a possibility to repair the error. Also, speed should be incorporated into the measure of risk as higher speed will cause greater damage.

Due to the intention of the framework is to be run realtime, some suggestions to improvements are mentioned. First off, the FM simulations some time compute. It is therefore time to save by using a smart OCA frequency logic. In addition to being based on the time since last simulation, it can also be dependent on exterior factors such as changes in the environment, weather forecasts and other vessels appearing on the AIS (Automatic Identification System). There is also room for improvement for the implmented A* algorithm, especially in the heuristic function which currently does not take the cost of risk into consideration. Other suggestions to A*'s runtime are mentioned in Patel (2019).

Improving usefulness of the results To make the method applicable, the calculation of risk must change. The new method should incorporate the time needed to achieve a certain consequence level (CL) within the failure mode simulations.

Given that the CL continues to only be defined by the distance to an obstacle, they should have more refined intervals in order to give more diverse risk levels. The different distances could then be based on how far the vessel can travel during a given failure mode during certain external forces, as this give the consequence levels some root in reality. A*'s cost of risk movement could then vary based on what consequence level the vessel might be in, as seen in Figure 5.2. This would provide greater flexibility to the framework.

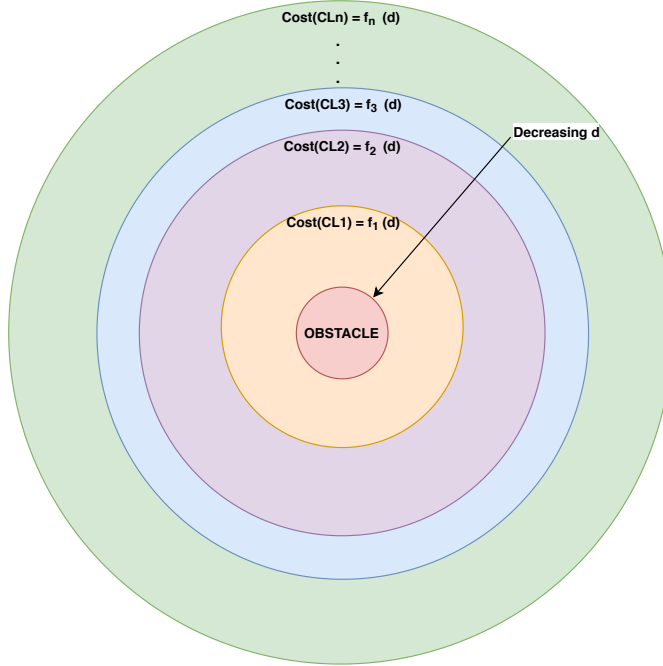


Figure 5.2: Multiple consequence levels with individual cost functions to be used in A*.

Chapter 6

Conclusion

The research question was: "*Can a ship's probabilities for partial system failure be updated automatically during the ship's transit due and can the risk of system failure be used to suggest new, safer routes?*"

The main outcome of the work is the integration of Online Consequence Analysis (OCA), a Bayesian Network and a modified A* path planning algorithm into a vessel simulator. The path planner activates when a certain risk level is reached and proposes new paths, as can be seen in Figure 4.14. The implementation of Online Consequence Analysis (OCA), a Bayesian Network (BN) and the A* path planning algorithm was successful in the purpose of lowering the chosen metric for risk by a small amount during simulation. By comparing the different paths chosen by the framework and ordinary LOS guidance it is observed that the framework is able to avoid collision while ordinary LOS is not. In spite of the small changes in the chosen risk metric, the new path looks to be considerably safer by visual inspection.

Hence, the answer to the research question based on the work presented in this thesis is "most likely".

List of Figures

2.1	Illustration of the ambition of the OCA framework.	9
2.2	Motion control system with integrated OCA and collision avoidance. The symbols are later explained in Section 2.4. Retrieved from Fos- sdal (2018).	11
2.3	The relation between latitude and longitude in the NED frame. Re- trieved from https://www.basicairdata.eu	12
2.4	The body frame for a marine vessel, with linear position x_b, y_b and z_b , angular velocities p, q, r and linear velocities u, v, w . Retrieved from Fossen (2011).	13
2.5	Illustration of the relationship between the NED frame and the body frame in 2D. X_b and Y_b are the x and y-directions in the body frame, respectively, while ψ is the yaw angle. Adapted from Fossdal (2018).	14
2.6	Part of the used map as it appears on NMA's online portal. Only the data in Table 2.4 are displayed.	20
2.7	The processing of map data	21
2.8	Comparison of different path planning algorithms	22
2.9	Flowchart of the A* algorithm	24
2.10	Principle behind LOS steering	26
2.11	Direced, undirected and cyclic graphs	27
3.1	Overview over the system used in the thesis	29
3.2	Applied Bayesian Network displayed in the GeNie Modeller	32
3.4	A* grid processing	36
4.1	Comparison between simplified model and simulation model	40
4.5	Validation: simulations of FM 1.	43
4.6	Validation: simulations of FM 2	44
4.7	Validation: simulations of FM 3.	45
4.8	Validation: simulations of FM 4.	46
4.9	Validation: resulting consequence levels for the different failure modes.	47
4.10	Changes in risk and most important failure mode for the simulation in Figure 4.1.	47
4.11	Probabilities for different failure modes with constant current.	49
4.12	Probability for different failure modes with varying current.	50

4.13	A* paths with different movement cost	51
4.14	NED plot of simulation with A* and BN boosted OCA.	53
4.15	Zoomed NED plot of simulation with A and BN boosted OCA showing different pathing.	54
4.16	Another zoomed NED plot of simulation with A and BN boosted OCA showing difference pathing.	55
4.17	Comparison of the perceived risk for the simulation in Figure 4.14 and the failure mode contributing to the highest amount of risk. . .	56
5.1	Method for handling inaccuracy in the simplified simulation model .	59
5.2	Multiple consequence levels with individual cost functions to be used in A*.	60

List of Tables

2.2	Lighting conditions at winter solstice in Gudvangen. Percentages for allision and grounding are retrieved from Stornes (2015) and represent the accidents for all ship types in NMA's accident database. Retrieved from Rasmussen (2019)	7
2.3	Distribution of wind force within accident types. Table 7.3.5 in Stornes (2015). N = 5997.	7
2.4	Map information defining the obstacles. Source: Geonorge.	20
3.1	Used failure modes and their static probabilities when the BN is not in use.	30
3.2	Consequence levels determined by the distance to the nearest obstacle and thresholds used in the simulations	31
3.3	The logic behind setting evidence for the current nodes in the bayesian network	33
3.4	A* movement costs	35
4.1	The Bayesian network's static evidence for different nodes.	49
4.2	Simulation parameters	52
A.1	Ship-level analysis of deficiency trajectory (Cariou et al., 2008). . .	71

Bibliography

- Christine Chauvin, Salim Lardjane, Gaël Morel, Jean-Pierre Clostermann, and Benoît Langard. Human and organisational factors in maritime accidents: Analysis of collisions at sea using the hfacs. *Accident Analysis Prevention*, 59:26 – 37, 2013.
- Mica R. Endsley. Situation Awareness Global Assessment technique (SAGAT). *Proceedings of the IEEE 1988 National Aerospace and Electronics Conference*, 1988.
- A. Wardzinski. Dynamic risk assessment in autonomous vehicles motion planning. In *2008 1st International Conference on Information Technology*, pages 1–4, May 2008. doi: 10.1109/INFTECH.2008.4621607.
- Carl E. B. Rasmussen. A top-down approach for making a marine vessel autonomous in order to reduce risk, 2019.
- Markus Fossdal. Online consequence analysis of situational awareness for autonomous vehicles. MSc thesis, Norwegian University of Science and Technology, 2018.
- Per Hokstad, Erik Jersin, and Terje Sten. A risk influence model applied to north sea helicopter transport. *Reliability Engineering and System Safety*, 74:311–322, 2001.
- Marvin Rausand. *Risk Assessment*. Wiley, 2011.
- Pierre Cariou, Maximo Q. Mejia, and Francois-Charles Wolff. On the effectiveness of port state control inspections. *Transportation Reserch Part E*, 44(3):491–503, 2008.
- Abbas Harati-Mokhtari, Alan Wall, Phillip Brooks, and Jin Wang. Automatic Identification System (AIS): Data Reliability and Human Error Implications. *The Journal of Navigation*, 60:373–389, 2007.
- Anita M. Rothblum. Human error and marine safety. Accessed: 11.02.2019, 2006.
- Olav F. Knudsen and Bjørn Hassler. IMO legislation and its implementation: Accident risk, vessel deficiencies and national administrative practices. *Marine Policy*, 35:201–207, 2010.

- Allianz Global Corporate & Speciality (AGCS). Safety and shipping 1912-2012. https://www.agcs.allianz.com/assets/PDFs/Reports/AGCS_safety_and_shipping_report.pdf, 2012. Accessed: 11.02.2019.
- Per Stornes. Risk influencing factors in maritime accidents. Technical report, NTNU Social Research, 2015.
- Asgeir J. Sørensen Eirik Mathiesen Torstein I. Bø, Tor A. Johansen. Dynamic consequence analysis of marine electric power plant in dynamic positioning. *Applied Ocean Research*, 57, 2016.
- Prabhakar V. Varde and Michael G. Pecht. *Risk-Based Engineering*. Springer, 2018.
- Thor I. Fossen. *Handbook of Marine Craft Hydrodynamics and Motion Control*. Wiley, 2011.
- GISGeography. Latitude, longitude and coordinate system grids, 2019. Retrieved 13.06.2019 at 19:18 from <https://gisgeography.com/latitude-longitude-coordinates/>.
- Asgeir J. Sørensen. TMR4240 - Marine Control Systems.
- Tristan Perez and Thor I. Fossen. Kinematic models for manoeuvring and sea-keeping of marine vessels. *Modelling, Identification and Control*, 28(1):19–30, 2007.
- W. E. Cummins. The impulse response function and ship motions. *David Taylor Model Basin*, 1962.
- Edward V. Lewis. *Principles of Naval Architecture (Second Revision), Volume II - Resistance, Propulsion and Vibration*. Society of Naval Architects and Marine Engineers (SNAME), 1988.
- Odd M. Faltinsen. *Sea Loads on Ships and Offshore Structures*. Cambridge University Press, 1990.
- Odd M. Faltinsen. *Hydrodynamics of high-speed marine vehicles*. Cambridge University Press, 2005.
- Randal W. Beard and Timothy W. McLain. *Small Unmanned Aircraft: Theory and Practice*. Princeton University Press, 2012.
- Kartverket. Tide tables for the norwegian coast and svalbard 2018. <https://kartverket.no/en/sehavniva/data-pa-se-havniva/Tide-Tables/>, 2018. Accessed: 16.06.2019.
- Alexandros Maratos. Towards ecdis mandatory carriage. <https://www.hydro-international.com/content/article/towards-ecdis-mandatory-carriage-2>, 2008. Accessed: 12.05.2019.

Per Arvid Jakobsen. Email exchange with retired senior engineer from kartverket, 2019.

Amit Patel. Amit's A* pages. <http://theory.stanford.edu/~amitp/GameProgramming/>, 2019. Accessed: 18.04.2019.

LLC BayesFusion. *SMILE Wrappers - Programmer's Manual*, version 1.0.3, built 7/9/2018 edition, 2018.

Appendix A

Tables

Number of deficiencies	Never deficient	Sometimes deficient	Always deficient	Number of observations	Chi ² (prob.)
<i>Vessel age at time of PSC (%)</i>					
[0; 5[43.8	52.3	3.8	130	54.99
[5; 10[28.5	62.6	8.9	123	(0.000)
[10; 15[24.8	62.0	13.2	121	
[15; 20[24.7	63.3	12.0	158	
[20; 25[24.2	56.8	18.9	132	
[25; 30[15.3	55.9	28.8	111	
[30; ∞[26.6	54.7	18.7	64	
<i>Compliance with ISM Code in 1998 (%)</i>					
No	29.4	54.6	16.0	469	7.31
Yes	24.0	63.8	12.2	370	(0.026)
<i>Type of ship (%)</i>					
General cargo	27.0	57.1	15.8	366	53.02
Bulk carrier	21.7	64.3	13.9	230	(0.000)
Passenger	7.5	75.5	17.0	53	
Ro-ro passenger	15.0	75.0	10.0	20	
Chemical tanke	54.0	37.8	8.1	37	
Ro-ro cargo	52.6	31.6	15.8	38	
Oil tanker	37.5	58.3	4.2	24	
Refrigerated cargo carrier	46.7	40.0	13.3	15	
Container	38.9	55.6	5.6	18	
Others	21	63.2	15.8	38	
<i>Flag (%)</i>					
Antigua and Barmuda	23.1	61.5	15.4	52	60.39
Bahamas	12.2	70.7	17.1	41	(0.000)
Cyprus	22.2	66.7	11.1	36	
Denmark	41.2	51.5	7.3	68	
Finland	20.9	72.1	7.0	43	
Germany	44.3	53.4	2.3	88	
Malta	24.0	64.0	12.0	25	
Netherlands	37.5	55.0	7.5	80	
Norway	20.7	53.7	25.6	82	
Russia	19.1	60.3	20.6	141	
Others	25.1	57.4	17.5	183	
<i>All (%)</i>	27.1	58.6	14.3	839	

Table A.1: Ship-level analysis of deficiency trajectory (Cariou et al., 2008).

